The *Stenotrophomonas maltophilia* MntR miniregulon includes novel extracytoplasmic components and affects replication in *Acanthamoeba castellanii* phagosomes

Fulvia-Stefany Argueta-Zepeda[1,2], Javier Rivera[1], Julio César Valerdi-Negreros[1,3] https://orcid.org/0000-0001-7536-5483, Christopher Rensing[4] https://orcid.org/0000-0002-5012-7953, and Pablo Vinuesa[1] https://orcid.org/0000-0001-6119-2956

[1]Centro de Ciencias Genómicas, Universidad Nacional Autónoma de México (UNAM), Cuernavaca, Morelos, México
[2]Programa de Maestría y Doctorado en Ciencias Bioquímicas, UNAM, Mexico City, Mexico
[3]Programa de Doctorado en Ciencias Biomédicas, UNAM, Mexico City, Mexico
[4]Fujian Agriculture and Forestry University, Fuzhou, China.

Address correspondence to Pablo Vinuesa, vinuesa@ccg.unam.mx

Keywords: AlphaFold, protein structural models, metal-homeostasis, host-microbe interactions, intracellular replication, nutritional immunity

ABSTRACT

Manganese homeostasis is crucial for bacterial survival, particularly for opportunistic pathogens like Stenotrophomonas maltophilia that switch lifestyles between contrasting environments. This study elucidates the manganese homeostasis system in S. maltophilia strain Sm18, a Mexican environmental isolate, revealing a sophisticated network that includes both conserved and novel components. We focus on the MntR miniregulon, which comprises the well-known inner-membrane importer MntH and exporter MntP, regulated by the Mn2+-responsive MntR metalloregulator. However, it also contains a TonB-dependent receptor (TBDR) with a distinctive CQNC motif likely involved in Mn2+ coordination and a

periplasmic thioredoxin-fold protein (TFP). Both are coexpressed from a bicistronic operon under severe manganese and iron limitation and belong to novel families with a limited phyletic distribution. Transcriptomic profiling under varying manganese and iron concentrations revealed a tight interplay between these metals, emphasizing the ferrophilic nature of S. maltophilia and the differential expression of the MntR miniregulon core members. Additional transporters of the RND and CDF families were also modulated under dual metal limitation. Mutant analysis demonstrated that MntP is critical for survival, even at Mn levels that do not affect growth kinetics. MntH is required for optimal intracellular replication within Acanthamoeba castellanii phagosomes, highlighting its role in overcoming nutritional immunity. Our findings offer new insights into the remarkable adaptability of S. maltophilia to diverse environments, which contributes to its success as an opportunistic pathogen.

IMPORTANCE

Stenotrophomonas maltophilia is an emerging multidrug-resistant opportunistic pathogen of increasing clinical concern. Understanding its metal homeostasis mechanisms is crucial for unraveling its physiological adaptability in colonizing diverse niches and its pathogenicity. This study provides the first comprehensive characterization of the manganese homeostasis system in *S. maltophilia*, revealing novel extracytoplasmic components and regulatory mechanisms. The identification of a novel TBDR family with a CQNC motif, which is cotranscribed in an operon with a periplasmic TFP as part of the manganese miniregulon, was unexpected and likely represents a novel post-transcriptional mechanism of TBDR assembly or regulation. Furthermore, demonstrating MntH's importance in intracellular replication within amoebae provided crucial insights into *S. maltophilia*'s strategies for overcoming host nutritional immunity. These findings contribute to our fundamental knowledge of bacterial physiology and highlight potential targets for developing new therapeutic strategies against *S. maltophilia* and possibly other opportunistic pathogens.

INTRODUCTION

Stenotrophomonas maltophilia is a Gram-negative, non-fermentative bacterium recognized for its ecological versatility and opportunistic pathogenicity (1). It thrives in diverse

environments, including soil, water, plant rhizospheres, free-living amoebae, and diverse animal organs and cells, demonstrating remarkable adaptability to contrasting ecological niches (2–4). These bacteria can survive under harsh conditions, such as oligotrophic or metal-rich environments, and are highly resistant to disinfectants and multiple drugs due to robust biofilm formation and multiple efflux systems. Recent research has highlighted these adaptive mechanisms, showing how they enhance *S. maltophilia's* resilience and persistence in hospital environments (1, 5), making it one of the ten most prevalent microorganisms in hospital care units (6). This pathogen primarily impacts immunocompromised individuals, leading to, among others, respiratory tract, bloodstream, and urinary tract infections (1), posing a significant challenge in clinical settings due to its intrinsic resistance to multiple antibiotics (4, 7). However, scarce knowledge is available on the genes and mechanisms involved in *Stenotrophomonas* adaptation to host-associated and intracellular lifestyles in diverse host tissues and phagocytic cells, such as free-living amoebae (3, 8) and mammalian macrophages (9). In recent years, mounting evidence has revealed that professional phagocytes subject the phagocytosed bacteria to limiting or toxic concentrations of transition metals, limiting their proliferation in phagosomes, a process termed nutritional immunity (10). Homeostasis and balance of essential transition metals, such as manganese, iron, copper, and zinc, are crucial for various physiological processes (11, 12). Metallostasis is controlled by a coordinated network of allosteric metalloregulators, metal transporters, metal-binding proteins, and efflux pumps (13). These components work together to regulate the intracellular concentration of metals, ensuring they are available for essential functions without reaching toxic levels (14). Furthermore, the ability of bacteria to adapt to different environments is closely linked to their metal homeostasis capabilities, as they can vary widely in various niches. For instance, the liver is the primary storage site for manganese in the human body, with concentrations around ~10 μM (15). Similar levels prevail in mouse organs (16). In contrast, manganese levels in the serum are kept low, typically less than 10 nM (17). Moreover, the modulation of iron (Fe) and manganese (Mn) levels, along with other trace elements in different tissues during bacterial infections in mice, highlights the critical role of metal homeostasis in the establishment and progression of infections (16, 18).

Studies on *S. maltophilia* metallostasis have focused on iron homeostasis, highlighting its importance in bacterial virulence (19). In contrast, our knowledge of the molecular mechanisms underlying manganese homeostasis in *Stenotrophomonas* is limited to a single

transcriptomic study performed on *Stenotrophomonas* sp. MNB17, an organism isolated from a deep-sea mud sample in the western Pacific that removes Mn^{2+} by efficiently forming Mn-precipitates ($MnCO_3$ and Mn-oxides) at high Mn concentrations (20). However, manganese homeostasis has been well-studied in some Gram-positive and Gram-negative bacteria (21, 22). In these bacteria, a crucial component of manganese homeostasis is the inner-membrane manganese transporter protein MntH, which facilitates manganese uptake from the periplasm into the cytoplasm under limiting conditions (23). Conversely, the inner-membrane exporter protein MntP removes excess manganese, thereby maintaining intracellular levels within the optimal range (24). This process is regulated by various regulatory proteins and signaling pathways that sense the intracellular manganese levels and adjust the expression or activity of manganese transporters (25, 21, 26). The dual transcriptional regulator MntR is the most studied (24, 27). Furthermore, under manganese limitation and oxidative stress, an Mn^{2+}-scavenging pathway has been identified in *Burkholderia thailandensis*, comprising a newly discovered TonB-dependent outer membrane (OM) manganese transporter MnoT, and an Mn^{2+}-binding protein, TseM, secreted by a type VI secretion pathway (T6SS) (28), apparently unique to Burkholderia species (10).

The requirement for Mn^{2+} and Fe^{2+} varies greatly across bacterial species (21). *S. maltophilia* features an iron-centric metabolism, requiring iron for optimal growth and virulence (19, 29). However, Mn^{2+} becomes essential under oxidative stress or low iron availability (30), conditions that mirror the environments that *S. maltophilia* likely encounters as an intracellular opportunistic pathogen in phagosomes subjected to nutritional immunity (10, 31). This bacterium has been reported to survive in human epidermoid epithelial cells (32), human lung epithelium cells (33, 34), free-living amoebae (3, 8), and mammalian macrophages (9, 33). The divalent Mn^{2+}/Fe^{2+} transporter Nramp1 protein, located in the phagosomal membrane and ubiquitous in eukaryotes, plays a crucial role in nutritional immunity by depleting phagocytosed bacteria of these micronutrients. Interestingly, its bacterial homolog, MntH, is also essential in countering this stress by importing Mn^{2+} into bacterial cells (35, 36).

Here, we present a detailed genomic, evolutionary, and functional analysis of *Stenotrophomonas* manganese homeostasis systems, demonstrating their contribution to bacterial fitness in *Acanthamoeba castellanii* phagosomes for the first time. We identified the key components of the MntR miniregulon in *S. maltophilia* Sm18, a Mexican environmental isolate (4, 37), and subjected them to genetic and functional analysis. We show that the

Sm18Δ*mntP* deletion strain is susceptible to Mn^{2+} *in vitro*. We identified two new genes of the miniregulon organized in an operon encoding a TonB-dependent receptor (TBDR) containing a conserved CQNC motif and a periplasmic thioredoxin-fold protein (TFP), which have not been previously reported in other bacteria to be regulated by Manganese. Phylogenomic and comparative genomic analyses revealed that both proteins belong to novel families. Detailed studies of the AlphaFold structural models revealed key features of likely functional relevance. RNA-Seq-based transcriptome analyses performed under limiting iron and manganese concentrations revealed that the TBDR-TFP locus and *mntH* gene are derepressed, underscoring their importance in maintaining metal homeostasis in metal-restricted environments, such as the phagosomes of diverse phagocytes. We have recently reported that Sm18 can survive and replicate in acidified Rab7A-positive vacuoles of *Acanthamoeba castellanii* trophozoites (3). Here, we report that the *mntH* gene is expressed and required for optimal intracellular replication in the phagosomes of this free-living professional phagocyte.

RESULTS

Complete genome sequencing and annotation of *Stenotrophomonas maltophilia* ESTM1D_MKCAZ16_6a (Sm18). All experiments in this study were performed with *S. maltophilia* ESTM1D_MKCAZ16_6a (Sm18), a multidrug-resistant strain recovered from the sediments of a clean river in Morelos, Central Mexico (4). A full description of its complete genome sequence is provided in a companion paper (37). The Sm18 genome assembly was derived from short pair-end Illumina MiSeq (2 x 300 bp) reads and long MinION (Oxford Nanopore Technologies) reads and consists of a single circular chromosome of 4,482,207 bp. Gene calling and genome annotation were performed using NCBI's PGAP pipeline (38), identifying 3,970 CDSs encoding proteins and 24 pseudogenes. GenBank's genome sequence and annotation are available under accession CP146374, with associated BioProject and BioSample identifiers PRJNA1081934 and SAMN40194962, respectively. Average blast nucleotide identity (ANIb) analyses computed with GET_PHYLOMARKERS (39) and reported in (37) confirm that Sm18 is a *bona fide S. maltophilia* strain, as previously determined by multilocus sequence analysis and population genetics (4).

Manganese impact on *S. maltophilia* Sm18 growth kinetics in complex and defined media The first step in characterizing the manganese homeostasis system of Sm18 was to assess the strain's manganese tolerance. We ran 48-hour growth kinetics using complex Luria-Bertani (LB) and minimal MOPS (MM) medium with increasing $MnCl_2$ concentrations. FIG 1A shows that Sm18 grows in LB and MOPS up to 16 mM and 8 mM of $MnCl_2$, respectively. In both media, the culture's maximal growth rate and total yield remained unaffected, except at the highest concentrations at which Sm18 can grow in each medium. However, statistical analysis of the area under the curve (AUC) for population density (OD_{600}) data presented in FIG 1B revealed a significant decrease in growth in both media starting at 8 mM of $MnCl_2$, mainly due to the extended lag phase of each growth curve observed with increasing manganese concentration. These results indicate that Sm18 exhibits notably higher tolerance to manganese than other Gram-negative bacteria like *E. coli* (40).

Genome-wide identification of manganese-responsive genes in *S. maltophilia* Sm18 by RNA-seq analysis under varying manganese and iron concentrations Our next goal was to identify the differentially expressed genes in the Sm18 genome under manganese limitation, sufficiency, and moderate surplus conditions. Given our interest in identifying Sm18 genes required for intracellular replication in *Acanthamoeba* phagosomes, a compartment that we hypothesize might limit both Mn^{2+} and iron Fe^{2+} availability to the containing bacteria, we analyzed the transcriptional profile of Sm18 under varying concentrations of both transition metals with RNA-sequencing (RNA-Seq).

The experiments and downstream analyses were conducted using three biological replicates of *Sm18* cultures grown in defined MM medium supplemented with casamino acids, under four contrasting combinations of Fe^{2+} and Mn^{2+} in micromolar (µM) concentrations: (i) Fe0 Mn0, (ii) Fe0 Mn8, (iii) Fe10 Mn0, and (iv) Fe10 Mn8. Principal component analysis (PCA) in FIG 2A demonstrated that replicates within each group were clustered and separated according to metal concentration. As reflected in PC1, 64% of the variance relates to varying iron conditions, while PC2 explains 10% of the variance due to manganese concentrations. Consequently, we anticipate more differentially expressed genes (DEGs) in response to changes in iron compared to manganese, supporting the classification of Sm18 as belonging to the group of bacteria with an iron-centric metabolism. To validate this statement, we

conducted a differential gene expression analysis using DESeq2. We identified a total of 124 differentially expressed genes (DEG) when comparing Fe^{2+} 10 µM vs Fe^{2+} 0 µM in MM-Mn0, and 89 DEGs in MM-Mn8, based on an adjusted P-value (padj) < 0.01 and a $\log_2$ fold change $|(\log_2 FC)| \geq 1.0$ (see Methods). In contrast, only 5 DEG were detected when comparing Mn^{2+} 0 µM vs Mn^{2+} 8 µM in MM-Fe10, and 16 DEG in MM-Fe0. To gain deeper insights into the transcriptional regulation interplay between manganese and iron homeostasis systems in Sm18, we visualized the DEG number for each condition using an Venn diagram presented in FIG 2B. This diagram consists of four interconnected ovals, each representing the number of DEG under specific conditions mentioned above, illustrating overlaps to identify shared DEG across conditions. Our analysis revealed that 88 DEG are regulated solely by iron levels, irrespective of the manganese concentrations in the medium. A detailed analysis of these genes will be presented elsewhere (Argueta and Vinuesa, *in prep*.). Among the elements of the manganese miniregulon in Sm18, *mntP* is the only gene exclusively regulated by manganese concentrations in the medium, independent of iron levels (FIG 2B). In contrast, the expression of *mntH* is affected by any change in manganese or iron concentration in the medium (FIG 2B). The latter result aligns with previous reports that *mntH* transcription is regulated by MntR and Fur (21). Nine genes displayed a differential expression only when cultures were subjected to simultaneous Fe^{2+} and Mn^{2+} limitation, with their locus tags listed in FIG 2B. Two were down-regulated (blue-colored locus tags) under these conditions, while the remaining ones were up-regulated, as detailed below. Figure 2C highlights the DEG identified when comparing Mn^{2+} 0 µM and Mn^{2+} 8 µM in both MM-Fe10 and MM-Fe0 media (see supplementary data, Tables 1 and 2 for more details). These DEGs are represented as colored dots on the $\log_2$FC plots, and their corresponding genomic loci are indicated by green vertical bars along the Sm18 chromosome. The DEG's molecular gene ontologies (GOs) are highlighted in different colors on the $\log_2$ FC charts, with the transmembrane transport category (yellow points) being the most prevalent. FIG 2C also shows bar charts for the $\log_2$ FC values for the same loci and treatments for a better quantitative representation, including the InterProt-based annotations of each DEG. FIG 2C revealed that ORFs 2357, 2358, and 4008, encoding respectively a TonB-dependent receptor (TBDR), a thioredoxin-fold protein (TFP), and the well-known cytoplasmic membrane Mn exporter MntP, are the three genes showing the most significant $\log_2$ FC values, exceeding 2.8 units in absolute values. TBDR and TFP are circled and, with a few others mentioned below, are likely involved in the Sm18 transition metal homeostasis system under simultaneous manganese and iron

limitation.These proteins were subjected to additional bioinformatic, genetic, and functional characterization, as detailed in the following sections. Finally, in MM supplemented with 8 μM Mn^{2+}, *mntH* expression was repressed, whereas *mntP* showed a >3 Log_2FC increase, presumably to export excess cytoplasmic manganese. Furthermore, in the absence of iron supplementation, other genes were upregulated along with *mntP*, including two predicted transporter proteins whose annotations are shown in FIG 2C. In contrast, five genes primarily associated with transmembrane transport were downregulated together with *mntH* and orf2357-orf2358 (FIG 2C).

Genome-wide scanning for potential MntR binding sites identifies the core components of the MntR mini regulon in *S. maltophilia* Sm18. Several Mn^{2+}-responsive genes are known to be regulated by the MntR protein, the master allosteric manganese transport metalloregulator of the DtxR family (41), which recognizes a short inverted palindromic sequence in the 5' UTR region of target loci known as MntR-box. We performed iterative MEME (42) searches (see Methods) to identify potential MntR-boxes in the Sm18 genome. We used the 5' UTRs of the *mntH* (manganese importer of the NRAMP family) orthologs from nine complete *S. maltophilia* complex genomes to generate a MEME hidden Markov model. The corresponding MntR motif logo is shown in FIG 3A. MAST-based (42) genome-wide scanning of the Sm18 assembly with the MntR-box HMM revealed the presence of two additional MntR binding sites that defined two additional genomic loci potentially under MntR regulation. The first site maps 75 bp upstream of V8P27_002357, encoding a putative TonB-dependent receptor (TBDR) closely linked to the *mntR* (V8P27_002359) and *mntH* (V8P27_002360) genes. These genes share a bidirectional promoter, with the MntR-box positioned 10 bp upstream of the *mntH* translation initiation site. (FIG 3B), shown by RNA-seq to be the DEG with the highest log_2FC value of those displaying differential regulation specifically under both Mn^{2+} and Fe^{2+} limitation (FIGS 2B and 2C). The second site maps 247 bp upstream of *mntP* (V8P27_004008), encoding the key cytoplasmic membrane Mn^{2+} exporter MntP, which is differentially expressed in media with high Mn^{2+} irrespective of Fe^{2+} concentration. As in *E. coli*, *mntP* in Sm18 is preceded by a putative *yybP-ykoY-like* riboswitch (FIG 3C). Based on this evidence, we postulate that *mntH* and ORFs 2357 and 2358 in the first genomic locus (FIG 3B), and *mntP* (FIG 3C), form the core of a putative MntR miniregulon in *S. maltophilia* Sm18, similar to that defined by Waters et al.

(24) for *Escherichia coli*. Interestingly, the V8P27_002357 gene and the immediately downstream-located putative thioredoxin-fold protein (V8P27_002358, TFP), which is co-transcribed with the preceding TBDR, are not found in MntR regulons reported in other bacteria (43).

Phylogenomic analysis reveals the distribution of MntR miniregulon core members across the selected *Xanthomonadaceae.* A broader MAST scan using the MntR-box HMM described in the previous section was performed on 79 complete genomes of *Xanthomonadaceae* (1 *Pseudoxanthomonas* spp, 1 *Xanthomonas* spp., and 77 *Stenotrophomonas* spp.) revealed that the MEME motif was unique for these loci using a cutoff P-value ≤ $1e^{-7}$, which located motif hits only upstream of orthologs of the Sm18 V8P27_002357 (TBDR), *mntH,* and *mntP* genes. The number of identified MntR-boxes ranged between 0 and 4, suggesting that not all genomes contain the miniregulon. To analyze the distribution of the five MntR miniregulon core members described in the previous section (FIG 3), we used BLASTP searches against genome-specific databases to identify homologs. Next, we estimated a maximum likelihood species tree for the 79 genomes based on the concatenated supermatrix of a filtered subset of 226 optimal core-genome genes selected with GET_PHYLOMARKERS (39) out of 849 input core genes computed with GET_HOMOLOGUES (44). Finally, we mapped taxonomic information, the presence-absence data of BLASTP hits, and the count data of MAST hits for the MntR motif on the tree shown in FIG 4. This analysis revealed that the five MntR miniregulon core members are found across a large clade, including members from *S. maltophilia* to *S. indicatrix* and *S. lactitubi*. Interestingly, only the strains in this species clade share V8P27_002357 (TBDR) and V8P27_002358 (TFP) homologs. Members of the *Stenotrophomonas* genospecies 1 (4, 39) and the *S. rhizophila-S. bentonitica* complex contain the remaining three core members (MntR, MntH, and MntP), but lack the MntR-box motif upstream of the missing V8P27_002357 homolog. None of the *Stenotrophomonas* species branching off deeper in the phylogeny, like *S. acidaminiphila,* produced BLASTP hits to members of the core MntR miniregulon, nor MAST hits for the MEME MntR-box motif. In conclusion, the complete, five-member core MntR miniregulon was found to have a phylogenetic distribution restricted to a clade grouping members of the *S. maltophilia complex*, *S. indicatrix*, and *S. lactitubi*, as shown in FIG 4.

Expression of the *S. maltophilia* Sm18 MntR miniregulon core genes is modulated by iron and manganese concentrations. To validate the bioinformatic predictions supporting the existence of an MntR miniregulon in *S. maltophilia* complex genomes (FIGS 3 and 4), we constructed transcriptional fusions of the 5'-UTRs of each of the three core loci of Sm18 to the Green Fluorescent Protein (GFP) using the broad-host-range plasmid pSEVA327 (Sm18/327-2357_2358, Sm18/327-*mntH*, and Sm18/327-*mntP;* supplementary data, Table 4). FIG 5A presents the corresponding promoter activities measured over 40 hours as the area under the curve (AUC) of GFP relative fluorescence units (RFU), normalized to the population density (OD_{600}), in response to varying manganese and iron concentrations. Expression data for the Sm18/327-2357_2358 fusion (FIG 5A, first panel) revealed that the operon encoding the novel TonB-dependent receptor (*orf2357*) and thioredoxin-fold protein (*orf2358*) is expressed solely under Mn and Fe limitation (Mn^{2+} 0 μM, and Fe^{2+} 0 μM), confirming the RNA-seq data (FIG 2). It should be noted that MM contains trace amounts of iron (~1.6 ppm) from the casamino acids (CAA) supplement. However, no GFP signal was detected in MM containing Mn^{2+} 80 nM, either with 0 or 10 μM Fe^{2+}, indicating that 0.08 μM Mn^{2+} is sufficient to repress the locus expression. The expression profile of the Sm18/327-*mntH* fusion (FIG 5A, second panel) is characterized by a highly significant decline in activity negatively correlated with increasing Mn^{2+} concentration in the culture medium. However, a low activity was still measurable at 8 μM of Mn^{2+}. Significantly higher activity in the Sm18/327-*mntH* expression profile was observed at 10 vs. 0 μM Fe^{2+}, except when the medium contains 8 μM of Mn^{2+}. These results again reveal a strong relationship in Sm18 between manganese and iron homeostasis, specifically in manganese uptake systems. This confirms our RNA-seq data and is consistent with observations made in *E. coli* (45, 46). As expected, the expression profile of Sm18/327-*mntP* increased significantly in Mn^{2+} 8 μM, compared to Mn^{2+} 0μM, irrespective of whether the medium was depleted or supplemented with iron (FIG 5A, third panel), in line with the RNA-seq results. As shown in FIG 1, although the upper Mn^{2+} concentration (8 μM) used for these experiments is orders of magnitude below the threshold tolerated by Sm18, it is sufficiently high to induce the cells to down-regulate the expression of importers and activate the MntP exporter to keep intracellular Mn homeostasis. In conclusion, these experimental data validated our RNA-seq results and bioinformatically derived

hypotheses regarding the presence of MntR-boxes upstream of core components of the *S. maltophilia* Mn homeostasis system.

The MntR metalloregulator controls the expression of core components of the Sm18 Mn homeostasis system. To confirm that the promoter activity observed in the transcriptional fusions reported in FIG 5A (previous section) is regulated by MntR, as suggested by the presence of potential MntR-boxes uncovered by our bioinformatic analysis (FIGS 3 and 4), the three fusions were transferred into an Sm18Δ*mntR* strain carrying a markerless *mntR* deletion (supplementary data, Table 3). Promoter activity in iron-deficient MM, with manganese concentrations of 0 μM and 8 μM, was measured as described in the previous section (FIG 5A). The Sm18ΔmntR/327-2357_2358 fusion (FIG 5B, first panel) revealed a significant increase in expression in the absence of supplemented manganese, suggesting derepression in the absence of the MntR transcription factor. However, adding manganese led to reduced expression, following a similar trend to that observed in the Sm18 wild-type background, suggesting that manganese may negatively regulate this operon via an alternative, MntR-independent mechanism. Similarly, derepression of the 327-*mntH* fusion was observed in the Sm18Δ*mntR* genetic background compared to the wild-type growing in MM without supplemented manganese (FIG 5B, second panel). However, no statistically significant activity was detected in the Sm18ΔmntR/327-*mntH* fusion upon adding 8 μM manganese. This suggests that manganese-dependent regulation of the *mntH* promoter activity is mediated exclusively through MntR. Finally, the *mntP* fusion exhibited manganese-dependent regulation exclusively through MntR, as no expression was detected in the absence of MntR, independently of manganese concentration, in line with the RNA-seq data (FIG 2).

In conclusion, the RNA-seq, bioinformatic, and transcriptional fusion analyses jointly and consistently confirm that MntR controls the expression of the three core components of the *S. maltophilia* Sm18 MntR miniregulon involved in manganese homeostasis. The *mntH* and *mntP* genes are highly conserved across Gram-negative and Gram-positive bacteria. In contrast, the bicistronic operon formed by the V8P27_002357 (TonB-dependent receptor) and V8P27_002358 (thioredoxin-fold protein) genes represent novel members of the MntR miniregulon not previously reported in other bacteria.

The V8P27_002357 TonB-dependent receptor belongs to a novel family with a restricted phylogenetic distribution and is characterized by a conserved CQNC motif in its plug domain, likely involved in metal coordination.

After confirming that the V8P27_002357 (TBDR) and V8P27_002358 (TFP) genes are members of the MntR miniregulon of *S. maltophilia sensu lato* strains (FIGS 3 and 4), and subjected to Mn^{2+} regulation (FIGS 2 and 5), we performed a detailed structural and phylogenomic characterization of these novel proteins to uncover structural features of potential functional significance and gain deeper insights into their potential function, evolution, and phylogenetic distribution. FIG 6 summarizes the findings for V8P27_002357. It encodes a 719 aa TonB-dependent receptor with a 28 bp-long N-terminal signal peptide, resulting in a mature protein of 76.6 kDa (691 aa) containing an N-terminal plug or core domain (141 aa, 15 kDa) featuring a centrally-located CQNC motif, followed by a TBDR β-barrel domain (550 aa, 61.6 kDa), as depicted in FIG 6A. We employed AlphaFold3 (AF3) (47) to uncover features of potential functional relevance from the modeled structure. A high-quality model was obtained (pTM = 0.93; mean pLDDT = 88.4). FIG 6C shows a side view of the mature apo protein's best-scoring model with three structural features of likely functional relevance highlighted in different colors (see figure legend): the TonB box (FIG 6B), the CQNC motif (FIG 6D), and one of the salt bridges, which might control substrate passage across the TBDR (FIG 6E). The CQNC motif is on the tip of a prominent antiparallel β-hairpin protruding toward the extracellular space from the plug domain (FIG 6D). The two cysteine thiol (sulfhydryl) side chains are close to each other (~3.1 Å; PAE = 1.54 Å (Predicted Alignment Error); FIG 6D inset), with the potential of forming a disulfide bond in the oxidizing periplasm's environment during the protein's transit to the outer membrane. The plug's N-terminal segment is disorganized and contains a potential TonB box motif (RVQVKV) predicted by the model to be hidden within the β-barrel (FIG 6C). This motif was identified by AF3 modeling (FIG 6B) of the complex formed by the 24 N-terminal residues of V8P27_002357 with the 80 C-terminal amino acids of the Sm18 TonB protein (V8P27_003890) forming its C-terminal domain (CTD), which revealed that the RVQVKV formed a parallel β-sheet with residues 71-76 of TonB's CTD (mean PAE 4.18 Å ± 0.38 SD). Furthermore, residue Arg19 following the Ton box forms a potential salt bridge with D332 located at ~2.5 Å (PAE = 2.07 Å) on the eighth β-strand (FIGS 6C, 6E), potentially forming an ionic lock (IL) that retains the Ton box within the β-barrel, as reported for BTUB_ECOLI, the *E.*

coli vitamin B12 TBDR (48, 49). The β-barrel domain displays the canonical structure of 22 antiparallel β-strands with short turns connecting strands on the periplasmic side and large loops and secondary structures oriented toward the extracellular space (FIG 6C).

Given that the expression of the V8P27_002357-V8P27_002358 locus is repressed by as little as 0.08 μM Mn^{2+} (FIG 5A), we also modeled the V8P27_002357 holoprotein with Mn^{2+} (FIG 6F). The AF3 model predicted with high certainty (ipTM = 0.84; pTM =0.90; mean pLDDT = 87.08) that the cysteines from the CQNC motif are involved in cation binding (FIGS 6F and 6G). To identify the coordinating donor atoms for Mn^{2+}, we searched for residues containing side chain atoms within 3.5 Å of the cation. This analysis revealed that the metal could be coordinated by two sulfur, one nitrogen, and one oxygen atom arrranged in a tetrahedral geometry (FIG 6H), contributed by residues C63, C66, E247, and H446 (FIG 6G) respectively, the latter two located on the β-barrel domain (FIG 6F). To challenge this hypothesis, we measured the distances between the donor atoms and the metal (FIG 6H) to compare them with those reported in the MESPEUS database of coordination groups in proteins (50), focusing on high-resolution structures (<= 1.8 Å). FIG 6I presents the distribution of the distances (as boxplots) between Mn^{2+} and the coordination donor atoms in Cys (median = 2.3245 ± 0.0259 median absolute deviation, n = 8), Glu (2.08 ± 0.1572, n = 53), and His (2.183 ± 0.2165, n = 66) residues extracted from the MESPEUS database as of March 2025, revealing that the measured coordination bond distances in V8P27_002357 (FIG 6H) are within the expected range, as computed from crystallography data, and very close to their median distances. Taken together, the high AF3 ipTM score, metal-donor distance measurements, and coordination geometry strongly suggest that residues C63, C66, E247, and H446 could be directly involved in metal coordination.

Interestingly, the AF3 model for the holoprotein with bound Mn^{2+} predicts an allosteric conformational switch, increasing the distance between the R19 and D332 residues (4.5 Å; PAE = 2.5; FIG 6J). This would release the IL, allowing the N-terminal sequence and TonB box to protrude from the β-barrel into the periplasmic space (FIGS 6F and 6J), presumably allowing contact with TonB's CTD. These findings are consistent with current mechanistic models for TonB transporters (49).

We used BlastP to search for V8P27_002357 homologs (excluding *Stenotrophomonas* hits) in the PDB, Swiss-Prot, and RefSeq selected protein databases. This analysis revealed a restricted and sparse phylogenetic distribution of the closest hits, which belong to a few

genera in the classes Bacteroidia, Flavobacteriia, Holophagae, Opitutia, Alphaproteobacteria, and Gammaproteobacteria. These sequences and the best hits found in PDB and Swiss-Prot were collected to generate a structure-guided multiple-sequence alignment and estimate a maximum likelihood phylogeny (see Methods). FIG 6K depicts a small summary tree, revealing that the closest V8P27_002357 homologs form a perfectly supported (100% bootstrap support) and tightly clustered lineage of sequences, all of them sharing the distinct CQNC motif in their plug domain (FIG 6L). Based on this structural and phylogenetic evidence, we propose that the V8P27_002357-like proteins comprise the new CQNC family of TBDRs (FIG 6K).

V8P27_002358 belongs to a novel family of periplasmic thioredoxin-fold proteins (pTFPs) linked to CQNC-type TBDRs by syntheny and co-expression, featuring a WC[AG]PC motif.

The presence of a periplasmic thioredoxin-fold protein (pTFP; matching IPR013766) co-expressed with a preceding CQNC-type TBDR (V8P27_002357 in strain Sm18) has not been previously reported and suggests that both proteins might be functionally related. To challenge this hypothesis, we first performed a phylogenomic and comparative genomic analysis of the locus. BLAST searching for V8P27_002358 homologs was done as described in the previous section for the V8P27_002357 TBDR, but extending the databases with the recently reported metagenomic dataset of thioredoxin superfamily proteins compiled by Nilewski et al. (51). The final dataset contained 203 proteins after removing nearly identical sequences by clustering at 99% of sequence identity with CD-HIT. A structure-guided multiple-sequence alignment was computed with mafft-dash, and a maximum likelihood phylogeny was estimated with IQTree. The resulting tree revealed that V8P27_002358 clustered in a highly supported and distinct clade (FIG S1) with uncharacterized sequences from a few genera belonging to the orders Lysobacterales (Gammaproteobacteria), Sphingomonadales (Alphaproteobacteria), and Opitutales (Verrucomicrobiota; Opitutia). We extracted the TFP homologs and flanking genes from the corresponding genome sequence of representative hits for synteny analysis. The V8P27_002358 clade members were found to be located immediately downstream of a CQNC-type TBDR (FIG 7A), strongly reinforcing the notion that they are functionally related. However, the genes flanking the TBDR-TFP locus were variable (FIG 7A).

V8P27_002358 is 173 aa long, featuring an N-terminal signal peptide of 23 aa (FIG 1B). The mature protein contains 159 aa, with a computed mass of 17.64 kDa and a periplasmic location, as predicted by Phobius (p = 0.94) and Psortb (score = 9.84). All TFPs share a minimal thioredoxin fold (TRX-fold) characterized by an N-terminal βαβ fold separated by an α-helix from the C-terminal ββα fold (52). The highly diversified and ubiquitous superfamily of TFPs (51, 53, 54) encode thiol:disulfide oxidoreductases (TDORs) that contain extra secondary structural elements and loops inserted between the conserved domains of the TRX-fold. Figure 7B displays the best-scoring AF3 model (pTM = 0.93; mean pLDDT = 92.35) computed for V8P27_002358. The conserved TRX-fold elements are color-coded (see figure legend). FIG 7B also displays the highly conserved CXXC (C40, C43) motif of thioredoxins and thioredoxin-like proteins found at the beginning of the α1 helix of the TRX-fold. The AF3 model for V8P27_002358 shown in FIG 7B presents the oxidized version of the CXXC motif (disulfide bridge in dark red). The protein contains an additional pair of cysteines at its C-terminus (C147, C154), also predicted to form a disulfide bond, as shown in FIG 7B. FIG 7C presents a 2D topological cartoon of the mature V8P27_002358 protein, highlighting the TRX-fold elements and the position of the short extra N-terminal α-helix (Eα1) and β-strands (Eβ1 and Eβ2), and the two extra C-terminal α-helices (Eα2 and Eα3). It has been well-established that the dipeptide flanked by the cysteines in the CXXC motif (55) and other neighboring residues constitute an extended active-site motif controlling the reactivity of TDORs (56). The V8P27_002358 protein contains an unusual CAPC dipeptide in the catalytic CXXC redox center. To gain further functionally relevant structural insight into the novel pTFPs associated with CQNC-type TBDRs (FIG 7A), we performed a motif analysis around the β1-α1 region of the TRX-fold, including well-characterized TFPs (SwissProt codes) with contrasting reduction potentials and pK_a values previously analyzed by Mavridou et al. (56). As shown in FIG 7D, there is considerable diversity in and around the CXXC motif dipeptide. The TFPs associated with the CQNC-type TBDRs are characterized by a distinctive and lineage-specific Y[FYC]GA[DS]WC[AG]PCH[AE]F[VL]P profile overlapping the CXXC motif, derived from the sequence logo shown in FIG 7D. Detailed inspection of the AF3 model around the CXXC motif of V8P27_002358 revealed that residues Y33 and A36, which are strictly conserved in the novel TFP family (FIG 7E), can establish hydrogen bonds with C39 and C42, potentially affecting their pK_a values and reactivity.

Mutants of MntR miniregulon members result in hydrogen peroxide and manganese sensitivity. To investigate whether the Sm18 *mntH* and *mntP* homolog encodes a functional manganese importer and exporter protein, we constructed the interrupted mutant Sm18VIMmntH and the markerless deletion mutant Sm18ΔmntP (see methods). The growth kinetics of the Sm18VIMmntH mutant indicate that the *mntH* gene is not essential under Fe^{2+}- or Mn^{2+}-limiting conditions in axenic cultures. However, it is required for growth under oxidative stress induced by hydrogen peroxide (H_2O_2), particularly at neutral pH (FIG 8A). Statistical analysis revealed that the difference in growth is significant only at 500 μM H_2O_2 (FIG 8B). These results are consistent with previous studies in bacteria, which demonstrated that *mntH* mutants are sensitive to H_2O_2, a phenotype largely attributed to their impaired ability to import manganese into the intracellular space (30). Conversely, it has been well established in diverse bacterial models that manganese exporter proteins are required to counter manganese toxicity (22, 40). Sm18Δ*mntP* was challenged with increasing concentrations of Mn^{2+} (5-160 μM; FIG 8C) and exhibited statistically significant sensitivity to manganese beginning at 40 μM, with complete growth inhibition observed at 160 μM (FIG 8D). The wild-type phenotypes of the Sm18VIM-*mntH* and Sm18Δ*mntP* strains were restored by plasmid pSEVA332 (Sm18VIM-*mntH*/332::*mntH* and Sm18Δ*mntP*/332::*mntP*), provided in trans and carrying the *mntH* and *mntP* genes under the control of their native promoters (FIG 8). These results demonstrate that *mntH* and *mntP* expression are essential for H_2O_2 resistance and manganese detoxification, respectively, and confirm that the uncovered MntR miniregulon is functional. It is noteworthy that the markerless mutants of genes V8P27_002357 and V8P27_002358 exhibited no phenotype under the tested conditions mentioned above.

The *S. maltophilia mntH* gene is expressed in *Acanthamoeba castellanii* phagosomes and is required for optimal intracellular replication. We recently found that *S. maltophilia* Sm18 resists digestion by *Acanthamoeba castellanii* strain Neff trophozoites and can replicate in acidified, Rab7A-positive *Stenotrophomonas*-containing vacuoles (SCV) of this free-living professional phagocyte (3). Given the fact that the phagosomes of *Dictyostelium discoideum* and human macrophages subject engulfed bacteria to iron and manganese limitation via the NRAMP exporter (57, 58), we postulated that the Sm18 MntH Mn importer would be required to survive in the *Acanthamoeba* SCV. To test this hypothesis, we first evaluated the expression of the transcriptional fusion of the *mntH* promoter region to mCherry2 by live-cell

imaging (LCI) of *A. castellanii* strain Neff cocultures with Sm18/pSEVA337R_mntH set at a multiplicity of infection of 25 (MOI25), using widefield fluorescence microscopy. As shown in FIG 9A, the fusion is expressed at 3 and 18 h post-primary contact (ppc). This result strongly suggests that phagocytosed Sm18 cells experience Mn, and possibly Fe limitation, in the SCV. We took advantage of our recently published *A. castellanii-Stenotrophomonas* co-culture assay using 96-well microtiter plates coupled to a fluorescence reader (3) to evaluate the replication capacity of the vector integration mutant (VIM) Sm18VIM*mntH* strain and the deleted mutant Sm18Δ*mntR* in amoebic trophozoites. We tagged Sm18VIM*mntH* and Sm18Δ*mntR* with our pUC18T_mTn7TC1_Pc_mScarlet-I minitransposon, which constitutively expresses the mScarlet-I fluorescent protein from the strong Pc promoter (3), resulting in strains Sm18VIM*mntH*::mTn7_Pc_mScarlet-I and Sm18Δ*mntR*::mTn7_Pc_mScarlet-I (supplementary data, Table 3). Its replication capacity in co-culture with Neff trophozoites was compared with Sm18 tagged with the same transposon (Sm18::mTn7_Pc_mScarlet-I). As shown in FIG 9B, the Sm18VIM*mntH* mutant has a statistically reduced replication capacity in Neff trophozoites, compared to Sm18, whereas Sm18Δ*mntR* exhibited growth capacity indistinguishable from the wild-type strain (FIGS 9B and 9C). These findings support the hypothesis that *Acanthamoeba* phagosomes restrict manganese availability to ingested bacteria and demonstrate that MntH is indispensable for optimal replication during intracellular life.

DISCUSSION

This study provides new insight into the MntR miniregulon of *Stenotrophomonas maltophilia* and related species in the *S. maltophilia* complex involved in manganese homeostasis, revealing similarities to known systems in other bacteria and novel cell envelope components. As expected, core elements of the *S. maltophilia* MntR system include the inner-membrane importer and exporter proteins MntH and MntP under the control of the MntR allosteric metalloregulator, which are highly conserved throughout evolution (24, 43). However, the *S. maltophilia sensu lato* lineage also features a novel bicistronic operon encoding an outer membrane (OM) TonB-dependent receptor (TBDR, V8P17_002357) and a periplasmic thioredoxin-fold protein (TFP, V8P17_002358). Gram-negative bacteria typically encode multiple TBDR-like genes, many with unknown functions (59, 60). It is well established that in *S. maltophilia,* iron limitation enhances virulence and biofilm formation (29, 61), and the

expression of TBDRs involved in heme (62), hemin (63, 64), and ferri-stenobactin (65, 66) uptake, as well as others involved in competition for secreted pyochelin siderophores in mixed cultures with *Pseudomonas aeruginosa* (67). Besides iron acquisition, *S. maltophilia* TBDRs have also been implicated in β-lactam (68) and keratin monomer uptake (69). *Xanthomonas*, the sister genus of *Stenotrophomonas*, features around 70 TBDRs, many of which are required for scavenging plant carbohydrates (59). At least 14 TonB-dependent iron acquisition and virulence pathways have been extensively studied in *P. aeruginosa* (70). Other well-known TBDRs like BtuB, OprC, FhuA, and FecA translocate vitamin B12 (cyanocobalamin), copper, ferric hydroxamate, and Fe^{3+} dicitrate, respectively. However, MnoT (Q2SY62_BURTA) from *Burkholderia* is the only TBDR currently known to import manganese (28). Analysis of the *S. maltophilia* Sm18 genome (37) revealed that it encodes for 65 putative TBDRs, representing one of this organism's most expanded paralogous gene families (data not shown). Our MEME-MAST analyses (FIG 3B) revealed that V8P27_002357 is the only TBDR associated with an MntR-binding box in Sm18. This box is located 75 bp upstream from the putative start codon, between the -10 and -35 regions (FIG 3B), supporting the notion that MntR is a transcriptional repressor of this locus. The transcriptional fusion and transcriptome profiling data revealed that the *orf002357-orf002358* operon derepressed only under severe manganese and iron restriction, with its expression virtually abolished upon addition of 80 nM of manganese. This correlates with observations of other TBDRs, typically expressed only under severely limiting nutritional conditions (28, 71), and highlights the interplay of manganese and iron in the unknown regulatory mechanism of the *orf2357-orf2358* locus. However, the Sm18Δ*orf2357* (TBDR) and Sm18Δ*orf2358* deletion mutants did not show a growth phenotype under these nutrient-restricted conditions, and the Sm18/337R-pr_*2357-2358* transcriptional fusion did not show activity in co-culture with *A. castellanii* trophozoites (data not shown). Phylogenomic analysis of the Sm18 TBDRs and a broad collection of well-classified reference proteins from this family revealed that it belongs to a novel clade possibly involved in Mn uptake, unrelated to the *Burkholderia* MnoT clade or typical iron-importing TBDRs mentioned above (data not shown). This conclusion is supported by the detailed analyses performed on the high-confidence alphaFold3 structural model generated for V8P27_002357. Its most distinguishing feature is the presence of a CQNC motif located on the tip of a loop connecting two antiparallel β-strands protruding from the plug domain toward the cell surface. Given the bioinformatic and transcriptional evidence gathered, we hypothesized that V8P27_002357 could function as an OM Mn importer. To

challenge this hypothesis, we modeled the binding of Mn^{2+} to V8P27_002357 with AlphaFold3 (AF3) (47). Detailed inspection of the high-confidence model obtained predicted, indeed, that the metal cation is coordinated with a tetrahedral geometry by the two cysteines from the CQNC motif and the spatially neighboring residues E247 and H446 from the β-barrel domain (FIGS 6F-H). Furthermore, the distances of these donor residues to the coordinated metal are all within the range of experimentally determined coordination distances in high-resolution (< 1.8 Å) crystal structures collected in the MESPEUS database of coordination groups in proteins (50) and close to the median distances computed from these structures (FIG 6I). Based on this strong modeling evidence, our current working hypothesis is that, in contrast to the MnoT-like TBDRs of Burkholderia, which require the T6SS-4-secreted Mn^{2+}-binding effector TseM to import the Mn^{2+}-TseM complex, in *S. maltophilia* Mn^{2+} might be directly coordinated in a tetrahedral geometry via the cysteines from the CQNC motif in the plug domain and the E247 and H446 residues from the β-barrel domain. Interestingly, we found that the potential salt bridge forming an ionic lock (IL) in the apoprotein model between R19 and D332 (FIGS 6C-E) could be released due to an allosteric switch upon ligand binding (FIGS 6F and 6J), possibly contributing to substrate import, as reported for the *E. coli* cianocobalamin transporter BtuB (48, 49), one of the extensively-characterized TBDRs with a relatively close phylogenetic relationship to V8P27_002357 (FIG 6K). This model prediction (FIGS 6D, 6E, 6G, 6J) is consistent with the experimental evidence provided by Hickman and colleagues via atomic force microscopy that BtuB's plug domain consists of an N-terminal mechanically weak subdomain. In contrast, the C-terminal subdomain is mechanically strong (72). According to this model, the N-terminal Ton box sequence gets exposed upon substrate binding and accessible for interacting with the periplasmic C-terminal domain (CTD) of the TonB protein, as reported for the *E. coli* BtuB transporter (73) and predicted by our AF3 model (FIGS 6B, 6F, and 6G). It has been proposed that the interaction between the Ton box and TonB's CTD contributes to partial plug unfolding by the pulling force exerted by the rotation of the inner membrane ExbBD motor (74). Taken together, the excellent fit of our AF3 model predictions with experimental data and models of TBDR function (48, 49, 71, 75) and the integral consideration of diverse structure confidence metrics (PAE, pILDT, ipTM, and pTM) lend strong support to our current functional model for V8P27_002357, and highlight the power of current AI protein structure prediction methods to generate highly accurate models and detailed working hypotheses for novel proteins (76). However, experimental evidence will be required to validate and refine the model predictions (77). This is particularly important for

membrane proteins such as TBDRs that establish multiple contacts with neighboring molecules in the densely crowded OM, which can affect folding details (49, 78).
The discovery of a periplasmic thioredoxin-fold protein (pTFP; V8P27_002358) as part of the MntR regulon expands the known components of bacterial manganese homeostasis and thiol-disulfide exchange systems. Furthermore, this finding adds a new layer of complexity to our understanding of how bacteria manage metal homeostasis and oxidative stress in the cell envelope. V8P27_002358's synteny, phylogenetic co-occurrence (FIG 7A), and co-transcription in a bicistronic operon with the preceding CQNC-type TBDRs suggest a functional coupling of both (V8P27_002357-2358) proteins. It is well established that most secreted proteins enter the periplasm via the Sec pathway in an unfolded state (79). The periplasm of Gram-negative bacteria is an oxidizing compartment in which the sulfur-containing amino acids cysteine and methionine are particularly vulnerable to oxidation by ROS (80). Disulfide bond formation in the periplasm of didermic Gammaproteobacteria is catalyzed by DsbA from the canonical DsbAB pathway as the unfolded intermediate transits through the SecYEG channel (81, 82). DsbA is a highly oxidizing soluble periplasmic oxidoreductase with a canonical thioredoxin fold and CXXC motif, which is also present in *S. maltophilia* Sm18 (V8P27_002985, BsbAsm). Therefore, it is likely that the two consecutive cysteines found in the CQNC-TBDR are oxidized, forming a disulfide bridge by the action of BsbAsm as it transits into the periplasm through the SecYEG channel. In this model, the cognate and specialized periplasmic thioredoxin-fold protein V8P27_002358 would be required to reduce the disulfide bond in the CQNC motifs as the protein folds and integrates into the outer membrane to fulfill its predicted role as a Mn-importing TBDR. This reduction is required for the two cysteines to participate in metal coordination, as predicted by the AF3 models presented in FIGS 6F-H and discussed above. Therefore, we postulate that V8P27_002358 is a specialized disulfide reductase for the CQNC motif in V8P27_002357. However, assuming this model is correct, it still raises the question of how the oxidized V8P27_002358 protein, after reducing its target's disulfide bond in the CQNC motif, is recycled back into its reduced state. One attractive and likely possibility is that the *S. maltophilia* Sm18 homolog (V8P27_003626; DsbDsm) of the inner membrane protein DsbD performs this reaction. DsbB is a promiscuous protein-disulfide reductase that works as a redox interaction hub, transferring electrons across the membrane from NADPH and the cytoplasmic Trx system via a cascade of thiol-disulfide exchange reactions to multiple periplasmic thiol-disulfide oxidoreductases (83, 84) belonging to diverse cell envelope

reducing pathways (85). This working model for the novel TBDR-pTFP locus opens up new avenues for research into bacterial metal acquisition strategies and thiol-disulfide homeostasis in the periplasm.

Regarding the conserved and broadly distributed MntR miniregulon components, this study reports the first genetic analysis of the *mntH* gene in *S. maltophilia*. It provides evidence that it encodes its primary manganese importer protein and is relevant for replication in amoebal phagosomes. Several lines of evidence support this conclusion. The *mntH* gene maps downstream of the *mntR* gene. It is regulated by both manganese and iron availability, as shown by our RNA-seq and transcriptional fusion data, and observed in *E. coli* and multiple other bacteria (43). Furthermore, transcriptome analysis suggests that no other manganese inner-membrane transporter is regulated solely by manganese availability in Sm18. Perhaps most significantly, *mntH* is reported herein for the first time to be required for *S. maltophilia*'s optimal replication within a professional phagocyte such as *Acanthamoeba castellanii*. This finding has broader implications for our understanding of *S. maltophilia*'s pathogenicity. It suggests that manganese acquisition contributes significantly to the bacterium's fitness within host cells. We observed active expression of the *mntH* promoter probe *in vivo* in co-cultures with *A. castellanii*. This indicates that Sm18 most likely faces manganese and iron restriction within the amoebal phagosomes. *S. maltophilia*'s ability to overcome these limitations through MntH-mediated manganese import may be a key factor in its success as an intracellular pathogen, as found in other bacteria (86–89), effectively overcoming the host's imposed nutritional immunity (10, 14), an ancient trait of eukaryotic phagocytes conserved from amoebae to macrophages (90). Given that *S. maltophilia*, like most Gammaproteobacteria, is a ferrophilic bacterium (see further discussion below), it is not surprising that the Sm18VIM*mntH* mutant did not display a significant impairment when grown in the defined MOPS medium without Mn (data not shown). This observation suggests that this mutant's attenuated replication rate in amoebal phagosomes might be due to its limited capacity to contend with reactive oxygen species (ROS), like superoxide anions and peroxide (30). Indeed, *S. maltophilia* genomes, including Sm18, encode a periplasmic Mn-dependent superoxide dismutase (SOD) and a Mn catalase (91). In addition, some enzymes like cambialistic SODs (92) or ribonucleotide reductases (45, 93, 94) can use either Fe or Mn as a co-factor, whereas mismetallation or oxidation via Fenton reactions of iron-containing enzymes in metal-restricted environments in the presence of ROS may be alleviated by using Mn as an alternative co-factor, as described for diverse mononuclear iron enzymes, most

notably the key enzyme ribulose-5-phosphate 3-epimerase (Rpe) from the pentose-phosphate pathway (PPP) (30, 95, 96). The metallation of Rpe with oxidative stress-resistant Mn^{2+} enables carbon flow through the PPP, producing the NADPH-reducing power required to maintain ROS-countering enzymes such as glutathione or thioredoxin reductase (97, 98) in the cytoplasm and diverse periplasmic disulfide isomerases and reductases, probably including the novel pTFP-encoding gene discovered herein.
This study did not directly analyze the links between Mn uptake and phagosome ROS contention in the *S. maltophilia-A. castellanii* interaction, which is the subject of current research in our laboratory. However, we did not identify DEGs associated with oxidative stress. This might result from using the wild-type rather than a mutant strain lacking manganese exporters.

In this study, we analyzed the links between manganese and iron homeostasis systems, focusing on the genes specifically induced by the former under the control of MntR and iron limitation. However, in addition to the MntR miniregulon members, a few other genes are differentially expressed under iron-replete and manganese-excess conditions. As anticipated, the *mntH* and *mntP* genes were differentially expressed. The remainder of the DEGs uncovered under these conditions require future investigation to validate their potential function in manganese and iron homeostasis. Of particular relevance was identifying some efflux pumps of the CDF and RND families, as they have generally been proposed as essential mechanisms for intracellular detoxification of zinc and copper during nutritional immunity (99), when iron and manganese concentrations are likely low. Moreover, emerging evidence indicates that the imbalanced ratio of transition metals can function as either a direct or indirect regulatory mechanism to mitigate metal toxicity through efflux pumps. The well-studied YiiP (CDF) has been identified in *Salmonella* Typhimurium as a secondary transporter in manganese export. Notably, its activity is not regulated by Fe or Mn concentrations in the medium, indicating that YiiP may play a role in balancing the levels of other metals (100). In *Streptococcus pneumoniae*, the expression of *czcD*, a zinc CDF efflux pump, is up-regulated under Mn(II)-limiting conditions (101). This is consistent with other studies showing that high zinc concentrations can compete with manganese binding sites on enzymes essential for cellular physiology (102). In *Bacillus subtilis*, reduced intracellular iron levels heighten the cells' sensitivity to elevated Co(II) or Mn(II), particularly in strains deficient in exporting these metals (103). Furthermore, disruption of the Mg(II) efflux system has been

observed to alleviate residual manganese toxicity in an *mntR mntH* mutant, likely by preventing mismetallation through Mg(II) accumulation (103, 104). In conclusion, we hypothesize that under manganese and iron limitation, in addition to uptake systems, other survival mechanisms of Sm18 involve transporters that re-establish the balance of transition metal pools by effluxing the most reactive ones with more favorable free energies (105, 106), thereby preventing mismetallation, as suggested in our integrative model (FIG S2). Our findings thus support the importance of maintaining a precise ratio of transition metals in bacterial physiology.

In conclusion, our comprehensive analysis of the manganese homeostasis system in *S. maltophilia* Sm18 revealed a sophisticated network of importers, exporters, and regulatory elements that work coordinately to maintain appropriate intracellular manganese levels. The identification of novel components, such as the TBDR and TFP, expands our understanding of bacterial metal homeostasis strategies and opens new avenues for future research. These findings advance our knowledge of *S. maltophilia* biology and contribute to the broader field of bacterial metal homeostasis, potentially informing new strategies for combating this and other opportunistic pathogens.

MATERIALS AND METHODS

Bioinformatic prediction of potential transcription factor binding sites We used the motif discovery algorithm MEME (v 5.3.3) from the MEME suite (42) to identify statistically overrepresented sequence motifs between 14 and 29 nucleotides long, located in the 5' UTR regions of *Stenotrophomonas mntH* (V8P27_002360) orthologs identified with GET_HOMOLOGUES (44). The resulting hidden Markov models (HMMs) were compared with entries in the CollecTF (107) and PRODORIC (108) databases of experimentally validated transcription factor-binding sites in Bacteria using TOMTOM (v 5.5.5) to determine the identity of the discovered motifs. The *Stenotrophomonas* motifs were iteratively refined by adjusting their lengths. The final HMMs were used by MAST (v 5.3.3) to scan complete genome sequences of *Xanthomonadaceae* to identify additional copies of the motifs in intergenic regions.

Bacterial strains and culture conditions *Stenotrophomonas maltophilia* ESTM1D_MKCAZ16_6a (Sm18) was isolated from sediments of the Las Estacas River in Morelos, Mexico (109). Sm18 was routinely cultivated under aerobic conditions in Luria-Bertani broth (10 g peptone, 5 g yeast extract, and 10 g NaCl in 1 L distilled water) at 30°C and 205 rpm or in MOPS, previously proven effective for cultivating *Pseudomonas* strains using 0.4 % (w/v) glucose as the carbon source (110). We optimized minimal medium MOPS (MM) for *S. maltophilia* growth by adding thiamine and biotin at 0.5% and 0.1% (w/v), respectively, along with 0.2% (w/v) Bacto™ casamino acids (CAA) to improve growth. Unlike the standard MOPS medium recipe, note that our MM lacks manganese in the micronutrient stock, as previous experiments in our laboratory have shown that nanomolar manganese concentration does not affect Sm18 growth. For the growth kinetics, the LB medium was supplemented with 10mM of MOPS buffer to maintain the pH above 6.5 after adding millimolar concentrations of manganese. The growth of Sm18 remained unaffected at this concentration of buffer and pH (data not presented). We cultured bacteria in MM supplemented with 30 µg/mg of chloramphenicol for the fluorescence kinetic analyses to select for plasmid pSEVA327.

Generation of markerless deletion mutants Two DNA genomic fragments, located upstream and downstream of the *mntP* gene, were amplified by PCR using total DNA from Sm18 as the template. The primer pair Sm18DmntP_PCR1.FOR and Sm18DmntP_PCR1.REV yielded a 570 pb fragment, while the pair Sm18DmntP_PCR2.FOR and Sm18DmntP_PCR2.REV produces a 512 pb fragment. These fragments were subsequently cloned into the pEX18Tc vector (111), previously linearized with EcoRI and HindIII, using NEBuilder HiFi DNA Assembly Master Mix from New England Biolabs (NEB), following the manufacturer's instructions. 10 µL of the resulting NEBuilder reaction were used to transform 50 µL of *E.coli* DH5α by heat shock. As the first step of plasmid confirmation, transformants were selected using blue-white screening. This was followed by PCR confirmation with the primers Sm18DmntP_PCR1.FOR and Sm18DmntP_PCR2.Rev, which amplifies a 1082 bp fragment. Finally, the plasmid was purified and linearized to confirm the size difference between the empty vector control and pEX18Tc::DmntP. The suicide vector pEX18Tc::DmntP was introduced into Sm18 by conjugation via *E. coli* S17 to obtain Sm18 merodiploids. Selection of Sm18 merodiploids was carried out using LB media supplemented with 20 µg/mL tetracycline and 30 µg/mL gentamicin and verified by colony PCR using a pair

of primers F24 and Sm18_VIM_mntP.R, which amplify the region from the insert plasmid to genomic DNA of Sm18. For the second homologous recombination, Sm18 merodiploids were grown in LB without NaCl and supplemented with 10% sucrose taken directly from glycerol. Marker-less deletion mutants were confirmed by tetracycline sensitivity, colony PCR using the primers Sm18DmntP_VER.F and Sm18DmntP_VER.R that amplified 1131 bp in Sm18 wild type and 570pb in Sm18Δ*mntP* mutant, and by sequencing—the same procedure generated markless TBDR, TFP, and mntH gene deletion mutants. See details of vectors and primers in supplementary Tables S4, S5 and S6.

Development of Interrupted Mutants A DNA fragment from the coding region of the *mntP* gene was amplified by PCR using total DNA from *Sm18* as the template. The primers Sm18-VIM-mntP.F1 and Sm18-VIM-mntP.R1 generated a 401 bp fragment, which was then cloned into the modified plasmid pEX18TcΔSacB-GFP. The insert and vector were linearized using BamHI and HindIII, followed by T4 DNA ligase (NEB) ligation according to the manufacturer's protocol. To introduce the construct, 10 µL of the ligation mix was used to transform 50 µL of *E. coli* DH5α by heat shock. Transformants were selected through blue-white screening, and the pEX18TcΔSacB-GFP_DmntP vector was verified by PCR using universal primers F24 and R24, which amplify a 522 bp fragment flanking the insert. As an additional confirmation, the vector was purified and linearized, and its size was compared to the empty vector control. The suicide vector pEX18TcΔSacB-GFP_DmntP was then introduced into *Sm18* by conjugation with *E. coli* S17, as previously described. The same procedure was used to generate interrupted mutants of the *TBDR* and *mntH* genes. See details of vectors and primers in supplementary Tables S4, S5 and 6.

Constructions of Sm18 expression plasmids We employ the empty backbone bacterial expression plasmids from pSEVA vector collection (112) for the construction of pSEVA327 and pSEVA337R bacterial expression plasmids, both harboring cassettes conferring chloramphenicol resistance. The former features an oriVRK2 facilitating replication at a low copy number across a broad host spectrum. It is replicated and maintained in most Gram-negative bacteria, and the cargo is a GFP expression module that lacks a promoter and is, therefore, well-suited for constructing expression plasmids. The latter encompasses an oriVpBBR1 of medium copy number and a mCherry expression module. Both contain an oriT that allows their transfer by conjugation if required. The intergenic area of V8P27_002357,

mntH, and *mntP* genes was amplified by PCR from genomic DNA using Phusion polymerase (NEB) and primers flanking 50-150 base pairs upstream and downstream, tagging with a restriction enzyme site for EcoRI, BamHI or HindIII. Subsequently, the vectors and amplicons were digested and ligated with T4 DNA polymerase (NEB) to generate the Sm18 expression plasmids 327-*TBDR_TFP*, 327-*mntH*, 327-*mntP*, 337R-*TBDR_TFP*, 337R-*mntH,* and 337R-*mntP*. See details of vectors and primers in supplementary Tables S4, S5 and S6.

Fluorescence kinetics and microbial growth The Fluorescence and growth kinetics were assessed across three or more biological replicates in a 96-well microplate. Bacterial optical density (OD_{600}) was adjusted to 0.05 in LB and 0.01 in MM-MOPS in a final volume of 200 µL of medium and supplemented with increasing $MnCl_2$ concentrations. For growth kinetics, cultures were grown at 30°C with orbital shaking at 205 rpm in a Biotek Epoch 2 microplate spectrophotometer, with OD_{600} readings taken every 30 minutes or 45 minutes. The same setup was utilized for fluorescence kinetics analysis, with fluorescence and growth measurements recorded using a BioTek Synergy H1 hybrid multi-mode microplate reader. Excitation and emission spectra for green fluorescent protein (GFP) were set at 479/12.5 nm and 520/12.5 nm, respectively.

Statistical analysis of fluorescence and growth kinetics For microbial growth curves, the uninoculated medium served as the blank. Meanwhile, for the fluorescence curves, besides subtracting the blank, normalization to the microbial growth was also conducted. The non-parametric Kruskal-Wallis test was used to compare the medians across independent groups based on the Area Under the Curve (AUC) derived from the growth or fluorescence measurements of Sm18 (or the specific strain/experiment name) to assess overall statistical significance. When significant differences were detected, post-hoc pairwise comparisons were performed using Dunn's test. The resulting *p*-values were adjusted for multiple comparisons using either the Bonferroni or Benjamini-Hochberg (BH) method, as appropriate. Significant contrast values were indicated on the figures using asterisks (*). The significance levels are as follows: $p > 0.05$ = ns (not significant); $p < 0.05$ = *; $p < 0.01$ = **; $p < 0.001$ = ***; $p < 0.0001$ = ****). The AUC was calculated using the Growthcurver package (v. 0.3.1). Bootstrapping was employed on the AUC data to compute 95% confidence intervals, which are represented as error bars in the corresponding figure. The rstatix package (v 0.7.2) was utilized to perform the statistical tests. All statistical analyses and graph generation were

conducted using the R programming language (v 4.3.2). Data variability was visualized using the ggplot2 (v 3.5.1) and ggpubr package (v 4.3.2). Error bars on the growth kinetic graphs represent the standard error of the mean for technical and biological replicates.

Cell sample preparation for RNA-sequencing Three biological replicates were obtained from glycerol stored at -80°C and cultured on agar LB to isolate colonies, with a one-day interval between each replicate. These cultures were then incubated at 30°C for 34 hours. Subsequently, a single isolated colony was subcultured in 3 mL of MM-MOPS and incubated at 30°C with agitation at 205 rpm for 24 hours. For pre-culturing, a 1:50 dilution was made in a final volume of 25 mL of MM-MOPS in a 50 ml Erlenmeyer flask and incubated at 30°C with shaking at 205 rpm for 14 hours. Following pre-culturing, 10 mL of preculture was collected by centrifugation (5000 x g for 5 minutes), washed three times with 5 mL of MM-MOPS without Fe (MM-Fe0), and resuspended in 5 mL of the same culture medium. This preculture was then used to inoculate 25 ml of four different micromolar metal-supplemented MM-MOPS media cultures at OD_{600} ~ 0.005: MM-Fe0Mn0, MM-Fe0Mn8, MM-Fe10Mn0 and MM-Fe10Mn8. For all conditions, Sm18 was incubated at 30 °C/205 rpm until reaching the early-log phase (OD_{600} 0.1 -0.2), after which the cultures were divided into two technical replicates and the cells were harvested by centrifugation as previously described. Immediately, the pellets were covered with 900µL of RNA later. One technical replicata was stored at 4°C until it was shipped to GENEWIZ from Azenta Life Science for library preparation and sequencing. The other was stored at -80°C for subsequent experiments. Standard RNA-seq was performed on the Illumina HiSeq 2500 platform, resulting in 150 bp paired-end reads.

RNA-seq analysis data and gene expression After read quality assessment using Fastqc v 0.12.1 (113), we employed Trimmomatic v 0.39 (114) to trim the index adapter and the initial 15 bp from each read, resulting in 135 bp reads and more than 23 million pair-end reads per sample. The complete genome sequence of *Stenotrophomonas maltophilia* strain ESTM1D_MKCAZ16_6a (BioProject: PRJNA1081934) served as a reference for aligning the reads using Bowtie2 v 2.4.4 (115). The aligned SAM files generated by Bowtie2 (overall alignment rate per sample >96%) were then used as input for featuresCounts from the R-Bioconductor software package Rsubreads v 2.14.2 (116). FeaturesCount generated an expression matrix containing the expression values of each sample for every gene using the

GFF genome annotation file (successfully assigned alignments per sample >92%). Differential gene expression analysis between conditions: Fe10Mn0 vs. Fe10Mn8, Fe0Mn0 vs. Fe0Mn8, Fe10Mn0 vs. Fe0Mn0 and Fe10Mn8 vs Fe0Mn8 were performed using DESeq2 v 1.42.0 (117), R-Bioconductor package which normalizes the raw counts through the median of ratios method and conducts differential expression analysis based on the negative binomial distribution of the data. DESeq2 adjusted P-values using Benjamini and Hochberg's method to reduce the false discovery rate. Differential Expression Genes (DEGs) were identified using the adjusted P-value (Padj) < 0.05 and log2 fold change > 1 or < -1 as cutoffs. The protein sequences of DGEs in response to Mn^{2+} stress under both iron-deficient and iron-supplemented conditions were analyzed using the UniProt database (https://www.uniprot.org), InterProScan (https://www.ebi.ac.uk/interpro/search/sequence/), and MOTIF search (https://www.genome.jp/tools/motif/) to assign gene ontology.

***Acanthamoeba castellanii* transcriptional fusion Sm18/337R-mntH co-culture for live-cell imaging (LCI) using widefield fluorescence microscopy** The detailed description of the procedure is found in Rivera 2024 (3). Briefly, co-cultures were established by seeding 20-mm diameter glass-bottom cell culture dishes with 5×10^5 *Acanthamoeba castellanii* strain Neff trophozoites, which were incubated for 1 hour at 30°C in MMsalts-MOPS-Glc medium. *Stenotrophomonas maltophilia* Sm18/337R-mntH was grown in LB medium, washed, and adjusted to an OD_{600} of ~1.0 (~4.8×10^8 CFUs/mL). Diluted bacterial suspensions were added to the culture dishes to achieve multiplicities of infection (MOI) 25, followed by centrifugation at 500 × g for 5 minutes to synchronize phagocytosis. LCI was performed on an AxioVertA1 inverted microscope (Karl Zeiss) at three and 18 h ppc.

Quantitative evaluation of the intracellular replication of mutants Sm18VIMmntH and Sm18Δ*mntR* using a microtiter plate assay The detailed description of the procedure is found in Rivera, 2024 (3). To evaluate the intracellular replication of the mutants Sm18VIMmntH::mTn7_Pc_mScarlet-I and Sm18Δ*mntR*::mTn7_Pc_mScarlet-I in *Acanthamoeba* trophozoites at MOI10, we used a microtiter plate assay that measured mScarlet-I fluorescence in co-cultures. Each well contained 1×10^5 trophozoites in MMsalts-MOPS-Glc, incubated for 30 minutes at 25°C. After replacing the medium with the tagged bacteria at the desired MOI, phagocytosis was synchronized by centrifugation at 500 × g for 5 minutes. The plates were then placed in the plate reader Synergy 2 and incubated

statically at 25°C. Red fluorescence was measured every 30 minutes for 48 hours at 568 nm/594 nm (excitation/emission). Controls included wells with medium, trophozoites in medium, or bacteria in medium.

ACKNOWLEDGEMENTS

We thank Alfredo Hernández and Víctor del Moral for their expert technical support and server maintenance at Centro de Ciencias Genómicas, UNAM. We acknowledge the excellent service provided by personnel at the Unidad de Síntesis y Secuenciación de DNA from Instituto de Biotecnología, UNAM. Dr. Ayari Fuentes from CCG-UNAM is thanked for providing access to the multimodal plate reader. A special thanks goes to Dr. Luis Lozano from the Bioinformatics Unit at CCG-UNAM for his advice and support during the early phase of transcriptome analysis. We thank M.Sc. Laura Cervantes for her laboratory assistance and valuable feedback. We gratefully acknowledge the financial support received from Consejo Nacional de Humanidades Ciencias y Tecnologías (CONAHCyT México, A1-S-11242), Secretaría de Ciencia, Humanidades, Tecnología e Innovación (SECIHTI México CBF-2025-I-1106), and Programa de Apoyo a Proyectos de Investigación e Innovación Tecnológica (PAPIIT), Universidad Nacional Autónoma de México (DGAPA-PAPIIT, UNAM: IN209321 and IN216424) to PV. F.S.A.Z and J.C.V.N. were recipients of CONAHCyT scholarships 659308 and 745705, respectively.

REFERENCES

1. Brooke JS. 2021. Advances in the Microbiology of Stenotrophomonas maltophilia. Clin Microbiol Rev 34:e00030-19.

2. Ryan RP, Monchy S, Cardinale M, Taghavi S, Crossman L, Avison MB, Berg G, Van Der Lelie D, Dow JM. 2009. The versatility and adaptation of bacteria from the genus Stenotrophomonas. Nat Rev Microbiol 7:514–525.

3. Rivera J, Valerdi-Negreros JC, Vázquez-Enciso DM, Argueta-Zepeda F-S, Vinuesa P. 2024. Phylogenomic, structural, and cell biological analyses reveal that

Stenotrophomonas maltophilia replicates in acidified Rab7A-positive vacuoles of *Acanthamoeba castellanii*. Microbiol Spectr 12:e02988-23.

4. Ochoa-Sánchez LE, Vinuesa P. 2017. Evolutionary Genetic Analysis Uncovers Multiple Species with Distinct Habitat Preferences and Antibiotic Resistance Phenotypes in the Stenotrophomonas maltophilia Complex. Front Microbiol 8:1548.

5. Brooke JS. 2012. Stenotrophomonas maltophilia: an Emerging Global Opportunistic Pathogen. Clin Microbiol Rev 25:2–41.

6. Rello J, Kalwaje Eshwara V, Lagunes L, Alves J, Wunderink RG, Conway-Morris A, Rojas JN, Alp E, Zhang Z. 2019. A global priority list of the TOp TEn resistant Microorganisms (TOTEM) study at intensive care: a prioritization exercise based on multi-criteria decision analysis. Eur J Clin Microbiol Infect Dis 38:319–323.

7. Chang Y-T, Lin C-Y, Chen Y-H, Hsueh P-R. 2015. Update on infections caused by Stenotrophomonas maltophilia with particular attention to resistance mechanisms and therapeutic options. Front Microbiol 6.

8. Denet E, Vasselon V, Burdin B, Nazaret S, Favre-Bonté S. 2018. Survival and growth of Stenotrophomonas maltophilia in free-living amoebae (FLA) and bacterial virulence properties. PLoS ONE 13:e0192308.

9. Takahashi I, Hosomi K, Nagatake T, Toubou H, Yamamoto D, Hayashi I, Kurashima Y, Sato S, Shibata N, Goto Y, Maruyama F, Nakagawa I, Kuwae A, Abe A, Kunisawa J, Kiyono H. 2020. Persistent colonization of non-lymphoid tissue-resident macrophages by *Stenotrophomonas maltophilia*. International Immunology 32:133–141.

10. Murdoch CC, Skaar EP. 2022. Nutritional immunity: the battle for nutrient metals at the host-pathogen interface. Nat Rev Microbiol 20:657–670.

11. Palmer LD, Skaar EP. 2016. Transition Metals and Virulence in Bacteria. Annu Rev Genet 50:67–91.

12. Waldron KJ, Robinson NJ. 2009. How do bacterial cells ensure that metalloproteins get the correct metal? Nat Rev Microbiol 7:25–35.

13. Porcheron G, Garénaux A, Proulx J, Sabri M, Dozois CM. 2013. Iron, copper, zinc, and manganese transport and regulation in pathogenic Enterobacteria: correlations between strains, site of infection and the relative importance of the different metal transport systems for virulence. Front Cell Infect Microbiol 3.

14. Chandrangsu P, Rensing C, Helmann JD. 2017. Metal homeostasis and resistance in bacteria. Nat Rev Microbiol 15:338–350.

15. Rahil-Khazen R, Bolann BJ, Myking A, Ulvik RJ. 2002. Multi-element analysis of trace element levels in human autopsy tissues by using inductively coupled atomic emission spectrometry technique (ICP-AES). Journal of Trace Elements in Medicine and Biology 16:15–25.

16. Kehl-Fie TE, Zhang Y, Moore JL, Farrand AJ, Hood MI, Rathi S, Chazin WJ, Caprioli RM, Skaar EP. 2013. MntABC and MntH Contribute to Systemic Staphylococcus aureus Infection by Competing with Calprotectin for Nutrient Manganese. Infect Immun 81:3395–3405.

17. Versieck J, Barbier F, Speecke A, Hoste J. 1974. Manganese, copper, and zinc

concentrations in serum and packed blood cells during acute hepatitis, chronic hepatitis, and posthepatitic cirrhosis. Clin Chem 20:1141–1145.

18. Pompilio A, Ciavardelli D, Crocetta V, Consalvo A, Zappacosta R, Di Ilio C, Di Bonaventura G. 2014. Stenotrophomonas maltophilia Virulence and Specific Variations in Trace Elements during Acute Lung Infection: Implications in Cystic Fibrosis. PLoS ONE 9:e88769.

19. Mikhailovich V, Heydarov R, Zimenkov D, Chebotar I. 2024. Stenotrophomonas maltophilia virulence: a current view. Front Microbiol 15:1385631.

20. Song F, Zhang G, Li H, Ma L, Yang N. 2022. Comparative transcriptomic analysis of Stenotrophomonas sp. MNB17 revealed mechanisms of manganese tolerance at different concentrations and the role of histidine biosynthesis in manganese removal. Ecotoxicology and Environmental Safety 244:114056.

21. Bosma EF, Rau MH, van Gijtenbeek LA, Siedler S. 2021. Regulation and distinct physiological roles of manganese in bacteria. FEMS Microbiology Reviews 45:fuab028.

22. Waters LS. 2020. Bacterial manganese sensing and homeostasis. Current Opinion in Chemical Biology 55:96–102.

23. Kehres DG, Zaharik ML, Finlay BB, Maguire ME. 2000. The NRAMP proteins of *Salmonella typhimurium* and *Escherichia coli* are selective manganese transporters involved in the response to reactive oxygen. Molecular Microbiology 36:1085–1100.

24. Waters LS, Sandoval M, Storz G. 2011. The Escherichia coli MntR Miniregulon Includes Genes Encoding a Small Protein and an Efflux Pump Required for Manganese

Homeostasis. J Bacteriol 193:5887–5897.

25. Wright Z, Seymour M, Paszczak K, Truttmann T, Senn K, Stilp S, Jansen N, Gosz M, Goeden L, Anantharaman V, Aravind L, Waters LS. 2024. The small protein MntS evolved from a signal peptide and acquired a novel function regulating manganese homeostasis in *Escherichia coli*. Molecular Microbiology 121:152–166.

26. Sengupta S, Mondal A, Dutta D, Parrack P. 2018. HflX protein protects Escherichia coli from manganese stress. J Biosci 43:1001–1013.

27. Que Q, Helmann JD. 2000. Manganese homeostasis in *Bacillus subtilis* is regulated by MntR, a bifunctional regulator related to the diphtheria toxin repressor family of proteins. Molecular Microbiology 35:1454–1468.

28. Si M, Zhao C, Burkinshaw B, Zhang B, Wei D, Wang Y, Dong TG, Shen X. 2017. Manganese scavenging and oxidative stress response mediated by type VI secretion system in *Burkholderia thailandensis*. Proc Natl Acad Sci USA 114.

29. Kalidasan V, Joseph N, Kumar S, Awang Hamat R, Neela VK. 2018. Iron and Virulence in Stenotrophomonas Maltophilia: All We Know So Far. Front Cell Infect Microbiol 8:401.

30. Anjem A, Varghese S, Imlay JA. 2009. Manganese import is a key element of the OxyR response to hydrogen peroxide in *Escherichia coli*. Molecular Microbiology 72:844–858.

31. Čapek J, Večerek B. 2023. Why is manganese so valuable to bacterial pathogens? Front Cell Infect Microbiol 13:943390.

32. Zhang T, Wu H, Ma C, Yang Y, Li H, Yang Z, Zhou S, Shi D, Chen T, Yang D, Li J, Jin M.

2024. Emergence of colistin-resistant Stenotrophomonas maltophilia with high virulence in natural aquatic environments. Science of The Total Environment 933:173221.

33. Nas MY, White RC, DuMont AL, Lopez AE, Cianciotto NP. 2019. Stenotrophomonas maltophilia Encodes a VirB/VirD4 Type IV Secretion System That Modulates Apoptosis in Human Cells and Promotes Competition against Heterologous Bacteria, Including Pseudomonas aeruginosa. Infect Immun 87:e00457-19.

34. DuMont AL, Karaba SM, Cianciotto NP. 2015. Type II Secretion-Dependent Degradative and Cytotoxic Activities Mediated by Stenotrophomonas maltophilia Serine Proteases StmPr1 and StmPr2. Infect Immun 83:3825–3837.

35. Juttukonda LJ, Skaar EP. 2015. Manganese homeostasis and utilization in pathogenic bacteria. Molecular Microbiology 97:216–228.

36. Cellier M. 2001. Polyphyletic origins of bacterial Nramp transporters. Trends in Genetics 17:365–370.

37. Vinuesa P, Fulvia-Stefany A-Z, Luz Edith O-S, Julio C. V-N, Mauricio D. O-H, Daniela G-H, Diana M. V-E, Javier R. 2024. Complete genome sequence of the environmental Stenotrophomonas maltophilia ESTM1D_MKCAZ16_6a (Sm18) strain recovered from sediments of a clean river in Morelos. Mexico, MRA.

38. Tatusova T, DiCuccio M, Badretdin A, Chetvernin V, Nawrocki EP, Zaslavsky L, Lomsadze A, Pruitt KD, Borodovsky M, Ostell J. 2016. NCBI prokaryotic genome annotation pipeline. Nucleic Acids Res 44:6614–6624.

39. Vinuesa P, Ochoa-Sánchez LE, Contreras-Moreira B. 2018. GET_PHYLOMARKERS, a

Software Package to Select Optimal Orthologous Clusters for Phylogenomics and Inferring Pan-Genome Phylogenies, Used for a Critical Geno-Taxonomic Revision of the Genus Stenotrophomonas. Front Microbiol 9:771.

40. Zeinert R, Martinez E, Schmitz J, Senn K, Usman B, Anantharaman V, Aravind L, Waters LS. 2018. Structure–function analysis of manganese exporter proteins across bacteria. Journal of Biological Chemistry 293:5715–5730.

41. Patzer SI, Hantke K. 2001. Dual Repression by Fe^{2+} -Fur and Mn^{2+} -MntR of the *mntH* Gene, Encoding an NRAMP-Like Mn^{2+} Transporter in *Escherichia coli*. J Bacteriol 183:4806–4813.

42. Bailey TL, Johnson J, Grant CE, Noble WS. 2015. The MEME Suite. Nucleic Acids Res 43:W39–W49.

43. Martin JE, Waters LS. 2022. Regulation of Bacterial Manganese Homeostasis and Usage During Stress Responses and Pathogenesis. Front Mol Biosci 9:945724.

44. Contreras-Moreira B, Vinuesa P. 2013. GET_HOMOLOGUES, a Versatile Software Package for Scalable and Robust Microbial Pangenome Analysis. Appl Environ Microbiol 79:7696–7701.

45. Wang NE, Courcelle EJ, Coltman SM, Spolek RL, Courcelle J, Courcelle CT. 2023. Manganese transporters regulate the resumption of replication in hydrogen peroxide-stressed Escherichia coli. Biometals 36:1361–1376.

46. Taudte N, German N, Zhu Y-G, Grass G, Rensing C. 2016. Restoration of growth by manganese in a mutant strain of Escherichia coli lacking most known iron and

manganese uptake systems. Biometals 29:433–450.

47. Abramson J, Adler J, Dunger J, Evans R, Green T, Pritzel A, Ronneberger O, Willmore L, Ballard AJ, Bambrick J, Bodenstein SW, Evans DA, Hung C-C, O'Neill M, Reiman D, Tunyasuvunakool K, Wu Z, Žemgulytė A, Arvaniti E, Beattie C, Bertolli O, Bridgland A, Cherepanov A, Congreve M, Cowen-Rivers AI, Cowie A, Figurnov M, Fuchs FB, Gladman H, Jain R, Khan YA, Low CMR, Perlin K, Potapenko A, Savy P, Singh S, Stecula A, Thillaisundaram A, Tong C, Yakneen S, Zhong ED, Zielinski M, Žídek A, Bapst V, Kohli P, Jaderberg M, Hassabis D, Jumper JM. 2024. Accurate structure prediction of biomolecular interactions with AlphaFold 3. Nature 1–3.

48. Zmyslowski AM, Baxa MC, Gagnon IA, Sosnick TR. 2022. HDX-MS performed on BtuB in E. coli outer membranes delineates the luminal domain's allostery and unfolding upon B12 and TonB binding. Proc Natl Acad Sci U S A 119:e2119436119.

49. Nilaweera TD, Nyenhuis DA, Cafiso DS. 2021. Structural intermediates observed only in intact Escherichia coli indicate a mechanism for TonB-dependent transport. Elife 10:e68548.

50. Lin G-Y, Su Y-C, Huang YL, Hsin K-Y. 2024. MESPEUS: a database of metal coordination groups in proteins. Nucleic Acids Res 52:D483–D493.

51. Nilewski S, Varatnitskaya M, Masuch T, Kusnezowa A, Gellert M, Baumann AF, Lupilov N, Kusnezow W, Koch M-H, Eisenacher M, Berkmen M, Lillig CH, Leichert LI. 2021. Functional metagenomics of the thioredoxin superfamily. J Biol Chem 296:100247.

52. Martin JL. 1995. Thioredoxin--a fold for all reasons. Structure 3:245–250.

53. Atkinson HJ, Babbitt PC. 2009. An atlas of the thioredoxin fold class reveals the complexity of function-enabling adaptations. PLoS Comput Biol 5:e1000541.

54. Anjou C, Lotoux A, Morvan C, Martin-Verstraete I. 2024. From ubiquity to specificity: The diverse functions of bacterial thioredoxin systems. Environ Microbiol 26:e16668.

55. Quan S, Schneider I, Pan J, Von Hacht A, Bardwell JCA. 2007. The CXXC motif is more than a redox rheostat. J Biol Chem 282:28823–28833.

56. Mavridou DAI, Saridakis E, Kritsiligkou P, Mozley EC, Ferguson SJ, Redfield C. 2014. An extended active-site motif controls the reactivity of the thioredoxin fold. J Biol Chem 289:8681–8696.

57. Peracino B, Buracco S, Bozzaro S. 2013. The Nramp (Slc11) proteins regulate development, resistance to pathogenic bacteria and iron homeostasis in Dictyostelium discoideum. J Cell Sci 126:301–311.

58. Morey JR, McDevitt CA, Kehl-Fie TE. 2015. Host-imposed manganese starvation of invading pathogens: two routes to the same destination. Biometals 28:509–519.

59. Blanvillain S, Meyer D, Boulanger A, Lautier M, Guynet C, Denancé N, Vasse J, Lauber E, Arlat M. 2007. Plant Carbohydrate Scavenging through TonB-Dependent Receptors: A Feature Shared by Phytopathogenic and Aquatic Bacteria. PLoS ONE 2:e224.

60. Schauer K, Rodionov DA, De Reuse H. 2008. New substrates for TonB-dependent transport: do we only see the ‘tip of the iceberg’? Trends in Biochemical Sciences 33:330–338.

61. García CA, Alcaraz ES, Franco MA, Passerini de Rossi BN. 2015. Iron is a signal for Stenotrophomonas maltophilia biofilm formation, oxidative stress response, OMPs expression, and virulence. Front Microbiol 6:926.

62. Shin HE, Pan C, Curran DM, Bateman TJ, Chong DHY, Ng D, Shah M, Moraes TF. 2024. Prevalence of Slam-dependent hemophilins in Gram-negative bacteria. J Bacteriol 206:e0002724.

63. Liao C-H, Lu H-F, Yang C-W, Yeh T-Y, Lin Y-T, Yang T-C. 2024. HemU and TonB1 contribute to hemin acquisition in Stenotrophomonas maltophilia. Front Cell Infect Microbiol 14:1380976.

64. Shih Y-L, Wu C-M, Lu H-F, Li L-H, Lin Y-T, Yang T-C. 2022. Involvement of the *hemP-hemA-smlt0796-smlt0797* Operon in Hemin Acquisition by Stenotrophomonas maltophilia. Microbiol Spectr 10:e00321-22.

65. Wu C-M, Li L-H, Lin Y-L, Wu C-J, Lin Y-T, Yang T-C. 2022. The sbiTRS Operon Contributes to Stenobactin-Mediated Iron Utilization in Stenotrophomonas maltophilia. Microbiol Spectr 10:e0267322.

66. Yeh T-Y, Lu H-F, Li L-H, Lin Y-T, Yang T-C. 2025. Contribution of fepAsm, fciABC, sbaA, sbaBCDEF, and feoB to ferri-stenobactin acquisition in Stenotrophomonas maltophilia KJ. BMC Microbiol 25:91.

67. Pan S-Y, Shih Y-L, Huang H-H, Li L-H, Lin Y-T, Yang T-C. 2022. The involvement of PacIRA system of Stenotrophomonas maltophilia in the uptake of Pseudomonas aeruginosa pyochelin and intraspecies competition for iron acquisition. Journal of

Microbiology, Immunology and Infection 55:273–281.

68. Calvopiña K, Dulyayangkul P, Heesom KJ, Avison MB. 2020. TonB-dependent uptake of β-lactam antibiotics in the opportunistic human pathogen Stenotrophomonas maltophilia. Mol Microbiol 113:492–503.

69. Xue K, Song X, Zhang W, Zhang Y, Chen T, Cao Z, Hong F, Zhang X. 2024. Omics-Based Investigation on Mechanisms Controlling Cellular Internalization of Keratin Monomers during Biodegradation by Stenotrophomonas maltophilia DHHJ. Microb Physiol 34:170–181.

70. Hubert T, Madec M, Schalk IJ. 2023. Experimental and computational methods to highlight behavioural variations in TonB-dependent transporter expression in Pseudomonas aeruginosa versus siderophore concentration. Sci Rep 13:20015.

71. Silale A, Van Den Berg B. 2023. TonB-Dependent Transport Across the Bacterial Outer Membrane. Annu Rev Microbiol 77:67–88.

72. Hickman SJ, Cooper REM, Bellucci L, Paci E, Brockwell DJ. 2017. Gating of TonB-dependent transporters by substrate-specific forced remodelling. Nat Commun 8:14804.

73. Shultis DD, Purdy MD, Banchs CN, Wiener MC. 2006. Outer membrane active transport: structure of the BtuB:TonB complex. Science 312:1396–1399.

74. Ratliff AC, Buchanan SK, Celia H. 2022. The Ton Motor. Front Microbiol 13:852955.

75. Braun V. 2024. Substrate Uptake by TonB-Dependent Outer Membrane Transporters.

Mol Microbiol 122:929–947.

76. Akdel M, Pires DEV, Pardo EP, Jänes J, Zalevsky AO, Mészáros B, Bryant P, Good LL, Laskowski RA, Pozzati G, Shenoy A, Zhu W, Kundrotas P, Serra VR, Rodrigues CHM, Dunham AS, Burke D, Borkakoti N, Velankar S, Frost A, Basquin J, Lindorff-Larsen K, Bateman A, Kajava AV, Valencia A, Ovchinnikov S, Durairaj J, Ascher DB, Thornton JM, Davey NE, Stein A, Elofsson A, Croll TI, Beltrao P. 2022. A structural biology community assessment of AlphaFold2 applications. Nat Struct Mol Biol 29:1056–1067.

77. Terwilliger TC, Liebschner D, Croll TI, Williams CJ, McCoy AJ, Poon BK, Afonine PV, Oeffner RD, Richardson JS, Read RJ, Adams PD. 2024. AlphaFold predictions are valuable hypotheses and accelerate but do not replace experimental structure determination. Nat Methods 21:110–116.

78. Nyenhuis DA, Nilaweera TD, Cafiso DS. 2020. Native Cell Environment Constrains Loop Structure in the Escherichia coli Cobalamin Transporter BtuB. Biophys J 119:1550–1557.

79. Smets D, Loos MS, Karamanou S, Economou A. 2019. Protein Transport Across the Bacterial Plasma Membrane by the Sec Pathway. Protein J 38:262–273.

80. Collet J-F, Cho S-H, Iorga BI, Goemans CV. 2020. How the assembly and protection of the bacterial cell envelope depend on cysteine residues. J Biol Chem 295:11984–11994.

81. Kadokura H, Beckwith J. 2009. Detecting folding intermediates of a protein as it passes through the bacterial translocation channel. Cell 138:1164–1173.

82. Landeta C, Boyd D, Beckwith J. 2018. Disulfide bond formation in prokaryotes. Nat Microbiol 3:270–280.

83. Katzen F, Beckwith J. 2000. Transmembrane electron transfer by the membrane protein DsbD occurs via a disulfide bond cascade. Cell 103:769–779.

84. Stirnimann CU, Grütter MG, Glockshuber R, Capitani G. 2006. nDsbD: a redox interaction hub in the Escherichia coli periplasm. Cell Mol Life Sci 63:1642–1648.

85. Bushweller JH. 2020. Protein Disulfide Exchange by the Intramembrane Enzymes DsbB, DsbD, and CcdA. J Mol Biol 432:5091–5103.

86. Champion OL, Karlyshev A, Cooper IAM, Ford DC, Wren BW, Duffield M, Oyston PCF, Titball RW. 2011. Yersinia pseudotuberculosis mntH functions in intracellular manganese accumulation, which is essential for virulence and survival in cells expressing functional Nramp1. Microbiology 157:1115–1122.

87. Anderson ES, Paulley JT, Gaines JM, Valderas MW, Martin DW, Menscher E, Brown TD, Burns CS, Roop RM. 2009. The Manganese Transporter MntH Is a Critical Virulence Determinant for *Brucella abortus* 2308 in Experimentally Infected Mice. Infect Immun 77:3466–3474.

88. Boyer E, Bergevin I, Malo D, Gros P, Cellier MFM. 2002. Acquisition of Mn(II) in addition to Fe(II) is required for full virulence of Salmonella enterica serovar Typhimurium. Infection and Immunity 70:6032–6042.

89. Zaharik ML, Cullen VL, Fung AM, Libby SJ, Kujat Choy SL, Coburn B, Kehres DG, Maguire ME, Fang FC, Finlay BB. 2004. The Salmonella enterica serovar typhimurium divalent cation transport systems MntH and SitABCD are essential for virulence in an Nramp1G169 murine typhoid model. Infect Immun 72:5522–5525.

90. Yu Y, Li Y-P, Ren K, Hao X, Fru EC, Rønn R, Rivera WL, Becker K, Feng R, Yang J, Rensing C. 2024. A brief history of metal recruitment in protozoan predation. Trends Microbiol 32:465–476.

91. Crossman LC, Gould VC, Dow JM, Vernikos GS, Okazaki A, Sebaihia M, Saunders D, Arrowsmith C, Carver T, Peters N, Adlem E, Kerhornou A, Lord A, Murphy L, Seeger K, Squares R, Rutter S, Quail MA, Rajandream MA, Harris D, Churcher C, Bentley SD, Parkhill J, Thomson NR, Avison MB. 2008. The complete genome, comparative and functional analysis of Stenotrophomonas maltophilia reveals an organism heavily shielded by drug resistance determinants. Genome Biol 9:R74.

92. Sendra KM, Barwinska-Sendra A, Mackenzie ES, Baslé A, Kehl-Fie TE, Waldron KJ. 2023. An ancient metalloenzyme evolves through metal preference modulation. Nat Ecol Evol 7:732–744.

93. Martin JE, Imlay JA. 2011. The alternative aerobic ribonucleotide reductase of Escherichia coli, NrdEF, is a manganese-dependent enzyme that enables cell replication during periods of iron starvation. Mol Microbiol 80:319–334.

94. Makhlynets O, Boal AK, Rhodes DV, Kitten T, Rosenzweig AC, Stubbe J. 2014. Streptococcus sanguinis class Ib ribonucleotide reductase: high activity with both iron and manganese cofactors and structural insights. J Biol Chem 289:6259–6272.

95. Sobota JM, Imlay JA. 2011. Iron enzyme ribulose-5-phosphate 3-epimerase in Escherichia coli is rapidly damaged by hydrogen peroxide but can be protected by manganese. Proc Natl Acad Sci U S A 108:5402–5407.

96. Imlay JA. 2014. The mismetallation of enzymes during oxidative stress. J Biol Chem 289:28121–28128.

97. Song M, Kim J-S, Liu L, Husain M, Vázquez-Torres A. 2016. Antioxidant Defense by Thioredoxin Can Occur Independently of Canonical Thiol-Disulfide Oxidoreductase Enzymatic Activity. Cell Rep 14:2901–2911.

98. Uppalapati SR, Vazquez-Torres A. 2022. Manganese Utilization in Salmonella Pathogenesis: Beyond the Canonical Antioxidant Response. Front Cell Dev Biol 10:924925.

99. Hood MI, Skaar EP. 2012. Nutritional immunity: transition metals at the pathogen–host interface. Nat Rev Microbiol 10:525–537.

100. Ouyang A, Gasner KM, Neville SL, McDevitt CA, Frawley ER. 2022. MntP and YiiP Contribute to Manganese Efflux in Salmonella enterica Serovar Typhimurium under Conditions of Manganese Overload and Nitrosative Stress. Microbiol Spectr 10:e01316-21.

101. Ogunniyi AD, Mahdi LK, Jennings MP, McEwan AG, McDevitt CA, Van Der Hoek MB, Bagley CJ, Hoffmann P, Gould KA, Paton JC. 2010. Central Role of Manganese in Regulation of Stress Responses, Physiology, and Metabolism in *Streptococcus pneumoniae*. J Bacteriol 192:4489–4497.

102. Sullivan MJ, Terán I, Goh KGK, Ulett GC. 2024. Resisting death by metal: metabolism and Cu/Zn homeostasis in bacteria. Emerging Topics in Life Sciences 8:45–56.

103. Pi H, Wendel BM, Helmann JD. 2020. Dysregulation of Magnesium Transport Protects

Bacillus subtilis against Manganese and Cobalt Intoxication. J Bacteriol 202.

104. Hohle TH, O'Brian MR. 2014. Magnesium-dependent processes are targets of bacterial manganese toxicity. Molecular Microbiology 93:736–747.

105. Osman D, Martini MA, Foster AW, Chen J, Scott AJP, Morton RJ, Steed JW, Lurie-Luke E, Huggins TG, Lawrence AD, Deery E, Warren MJ, Chivers PT, Robinson NJ. 2019. Bacterial sensors define intracellular free energies for correct enzyme metalation. Nat Chem Biol 15:241–249.

106. Irving H, Williams RJP. 1953. 637. The stability of transition-metal complexes. J Chem Soc 3192.

107. Erill I. 2015. Every Site Counts: Submitting Transcription Factor-Binding Site Information through the CollecTF Portal. J Bacteriol 197:2454–2457.

108. Dudek C-A, Jahn D. 2022. PRODORIC: state-of-the-art database of prokaryotic gene regulation. Nucleic Acids Research 50:D295–D302.

109. Ochoa-Sánchez LE, Vinuesa P. 2017. Evolutionary Genetic Analysis Uncovers Multiple Species with Distinct Habitat Preferences and Antibiotic Resistance Phenotypes in the Stenotrophomonas maltophilia Complex. Front Microbiol 8:1548.

110. LaBauve AE, Wargo MJ. 2012. Growth and laboratory maintenance of Pseudomonas aeruginosa. Curr Protoc Microbiol Chapter 6:Unit 6E.1.

111. Hoang TT, Karkhoff-Schweizer RR, Kutchma AJ, Schweizer HP. 1998. A broad-host-range Flp-FRT recombination system for site-specific excision of

chromosomally-located DNA sequences: application for isolation of unmarked Pseudomonas aeruginosa mutants. Gene 212:77–86.

112. Martínez-García E, Fraile S, Algar E, Aparicio T, Velázquez E, Calles B, Tas H, Blázquez B, Martín B, Prieto C, Sánchez-Sampedro L, Nørholm MHH, Volke DC, Wirth NT, Dvořák P, Alejaldre L, Grozinger L, Crowther M, Goñi-Moreno A, Nikel PI, Nogales J, de Lorenzo V. 2023. SEVA 4.0: an update of the Standard European Vector Architecture database for advanced analysis and programming of bacterial phenotypes. Nucleic Acids Research 51:D1558–D1567.

113. Andrews, S. 2010. Fastqc: A quality control tool for high throughput sequence data (v0.11.2). Babraham bioinformatics Institute, Cambridge, UK.

114. Bolger AM, Lohse M, Usadel B. 2014. Trimmomatic: a flexible trimmer for Illumina sequence data. Bioinformatics 30:2114–2120.

115. Langmead B, Salzberg SL. 2012. Fast gapped-read alignment with Bowtie 2. Nat Methods 9:357–359.

116. Liao Y, Smyth GK, Shi W. 2019. The R package Rsubread is easier, faster, cheaper and better for alignment and quantification of RNA sequencing reads. Nucleic Acids Research 47:e47–e47.

117. Love MI, Huber W, Anders S. 2014. Moderated estimation of fold change and dispersion for RNA-seq data with DESeq2. Genome Biol 15:550.

FIGURE LEGENDS

FIG 1. Growth kinetics of *S. maltophilia* Sm18 under increasing Mn concentrations. (A) Growth in Luria-Bertani (LB) and minimal MOPS (MM) medium with increasing millimolar (mM) concentrations of manganese (Mn). Means of eight biological replicates per concentration are represented by distinct shapes and colors, with error bars indicating the standard error. (B) Statistical analysis of Mn tolerance in Sm18. Differences among groups were assessed using the Kruskal-Wallis test followed by Dunn's post hoc test with Benjamini-Hochberg (BH) correction. Significance levels are shown as: ns, $P > 0.05$; *, $P < 0.05$; **, $P < 0.01$; ***, $P < 0.001$; ***, $P < 0.0001$. Black asterisks indicate comparisons against the manganese-free control, while red asterisks denote comparisons between other groups.

FIG 2. Transcriptomic analysis and identification of differentially expressed genes (DEGs). (A) Principal component analysis (PCA) based on DESeq2-normalized read counts from the full transcriptome (n = 4,059 genes). (B) Venn diagram generated using the VennDiagram package in R, illustrating the overlap of DEGs under different metal concentrations. Genes were considered differentially expressed if they met the criteria of adjusted P-value (padj) < 0.01 and $|\log_2$ fold change$| \geq 1$. (C) DEGs from Mn^{2+} 0 µM vs. Mn^{2+} 8 µM comparisons in MM-Fe10 and MM-Fe0 mapped across the Sm18 chromosome (Chr Sm18). Green loci denote regions with significant differential expression. Colored dots represent genes classified by Gene Ontology (GO) functional categories. The adjacent bar chart displays InterPro-based annotations of each DEG.

FIG 3. Core components of the MntR miniregulon in *S. maltophilia* Sm18. (A) Binding motif for the transcription factor MntR (MntR-box), identified using MEME. The MntR-box corresponds to a 16-bp palindromic sequence. (B) Putative manganese uptake operon encoding an outer membrane TonB-dependent receptor and a thioredoxin-fold protein, identified by locus tags 2357 and 2358, respectively. The MntR-box is located 75 bp upstream of the start codon, between the -10 and -35 promoter regions. These genes are adjacent to the *mntR* and *mntH* loci, which share the intergenic area or 117 pb. The *mntH* MntR-box is located 10 bp upstream of its start codon. (C) The locus that encoding an Inner membrane manganese exporter *mntP*, predicted to be regulated by both the *yybP-ykoY* riboswitch and MntR. Its MntR-box is located 247 bp upstream of the start codon.

FIG 4. Distribution of the core members of the MntR miniregulon in the family *Xanthomonadaceae*. Maximum-likelihood phylogenomic tree based on the concatenation of 226 core genes from 79 *Xanthomonadaceae* strains. The phylogeny integrates taxonomic information, the presence/absence of miniregulon genes (orf0235, orf02358*, mntH*, *and mntP*), the transcription factor mntR locus, and the number of MntR-boxes detected by MAST. The complete miniregulon shows a restricted distribution within the *S. maltophilia*, *S. indicatrix*, and *S. lactitubi*.

FIG 5 Statistical analysis of fluorescence intensity for transcriptional fusions of Sm18 genes

within the manganese MntR miniregulon. (A) Area under the curve (AUC) of normalized relative fluorescence units (RFU), corrected using the RFU of strains carrying the empty pSEVA-327 plasmid. Nine biological replicates were conducted in minimal medium MOPS (MM) supplemented with 30 µg/mL chloramphenicol. AUC values of transcriptional fusions Sm18/327-2357_2358, Sm18/327-mntH and Sm18/327-mntP are shown as mean ± 95% CI (bootstrap) for 0 and 10 µM Fe^{2+} conditions. Each Fe condition was tested with 0, 0.08 and 8 µM of Mn^{2+}. (B) AUC of normalized RFU for five biological and four technical replicates of Sm18 and Sm18ΔmntR strains harboring the same fusions grown in MM-Fe0. Differences were assessed using the Kruskal–Wallis test followed by Dunn's post hoc test with BH correction. Significance levels are shown as: ns, $P > 0.05$; *, $P < 0.05$; **, $P < 0.01$; ***, $P < 0.001$; ***, $P < 0.0001$. Black asterisks denote comparisons across Mn concentrations, red asterisks denote Fe comparisons, and gray asterisks indicate combined Fe/Mn variations.

FIG 6 Structural and phylogenetic analysis of the novel CQNC family of TBDRs. (A-E) Domain organization and AF3 models of V8P27_002357 showing the β-barrel (teal), plug domain (orange), and residues forming an ionic lock (R19-D332). (F-J) Mn^{2+}-bound AF3 models highlighting coordinating residues (C63, C66, E247, H446) and donor-metal distances from MESPEUS database and structural effects of ionic lock disruption upon Mn^{2+} binding. (K-L) Maximum-likelihood phylogeny and ESPript alignment showing the conserved CQNC motif characteristic of this TBDR family.

FIG 7 Comparative genomics of the TBDR-TFP locus and structural features of the thioredoxin-fold protein (TFP) V8P27_002358. (A) Multiple alignment showing conserved synteny of TBDR-TFP loci across Lysobacterales, Sphingomonadales, and Opitutales. Gray shading indicates sequence identity. Loci are ordered according to a neighbor-joining tree based on Mash distances. (B-C) AF3 models and 2D cartoon of V8P27_002358 showing canonical thioredoxin-fold organization (light blue and ruby units), oxidized CXXC motif (C39-C42) and secondary disulfide bridge (C147-C154).
(D-E) Structure-guided multiple-sequence alignment associated with CQNC-TBDRs and close-up of the CXXC motif showing residues predicted to form hydrogen bonds with catalytic cysteines (C39, C42).

FIG 8. Phenotypic characterization of *mntH* and *mntP* mutants of *S. maltophilia* Sm18.(A-B) Growth kinetics of the Sm18VIM-mntH mutant under oxidative stress induced by hydrogen peroxide (H_2O_2) at different pH values. The *mntH* mutant showed no growth defect under Fe^{2+}- or Mn^{2+}-limiting conditions but exhibited increased sensitivity to hydrogen peroxide (0.2 and 0.5 mM), particularly at neutral pH (orange triangles). (C-D) Growth kinetics of the markerless Sm18ΔmntP mutant exposed to increasing Mn^{2+} concentrations (5-160 µM). Deletion of *mntP* results in significant manganese sensitivity starting at 40 µM, with complete growth inhibition at higher concentrations. Complementation with plasmid pSEVA332 carrying *mntH* or *mntP* under their native promoters restored the wild-type phenotype (green cubes). Error bars represent SEM for growth kinetics and 95% CI (bootstrap) for AUC analysis for 3

biological replicates. Statistical significance was evaluated using the Kruskal–Wallis test with Dunn's post hoc BH correction: ns, $P > 0.05$; *, $P < 0.05$; **, $P < 0.01$; ***, $P < 0.001$; ****, $P < 0.0001$. Blue asterisks denote comparisons between wild type (blue circles) and mutants; orange asterisks indicate comparisons across H_2O_2 or Mn^{2+} concentrations.

FIG 9. Expression of the transcriptional fusion Sm18/337-mntH and intracellular replication of the Sm18VIM-mntH mutant in co-culture with *Acanthamoeba castellanii*. (A) Representative images from six biological replicates of co-cultures of Sm18/337R−mntH with *A. castellanii* trophozoites at 3 and 18 h post co-culture. Promoter activity is shown in the red filter (mCherry2), trophozoite vacuoles in bright field, and merged images at 10 µm scale. (B) Fluorescence kinetics of mScarlet-I-labeled strains: Sm18 (blue triangles), Sm18VIMmntH (orange cubes) and Sm18ΔmntR (green lines). Background fluorescence from medium-bacteria controls was subtracted for normalization. (C) Kruskal–Wallis test was used to compare medians between groups. When significant differences were detected, pairwise comparisons were performed using Dunn's test with Bonferroni correction. Significance levels: ns, $P > 0.05$; *, $P < 0.05$; **, $P < 0.01$; ***, $P < 0.001$; ****, $P < 0.0001$.

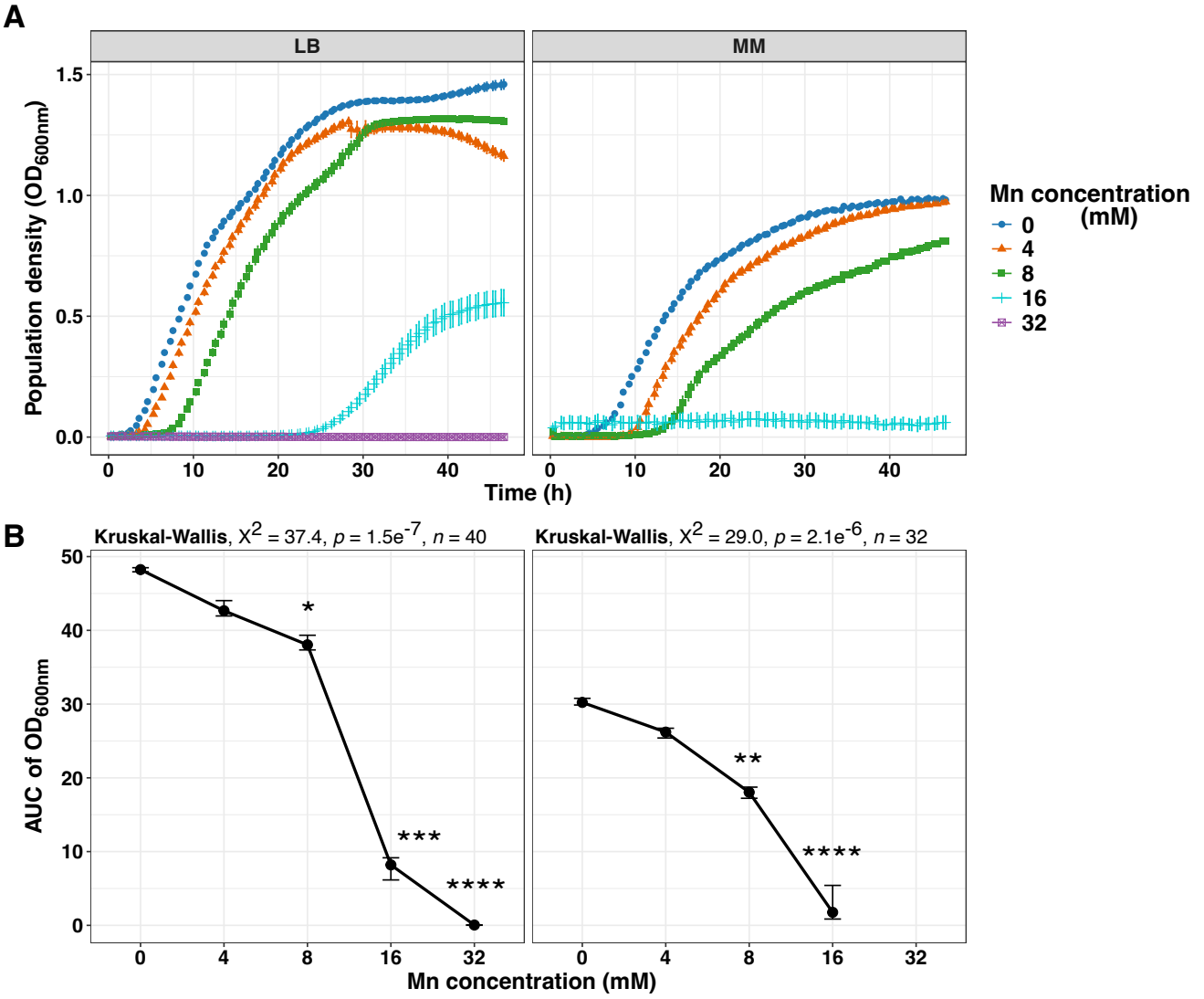

Evaluated contrasts

group1	group2	p.adj	p.adj.signif
0	8	1.101202e−02	*
0	16	1.470991e−04	***
0	32	4.379815e−07	****
4	16	1.101202e−02	*
4	32	1.470991e−04	***
8	32	1.101202e−02	*

group1	group2	p.adj	p.adj.signif
0	8	1.293498e−03	**
0	16	1.864407e−06	****
4	16	1.293498e−03	**

pwc: **Dunn test**; p.adjust: **Benjamini-Hochberg**

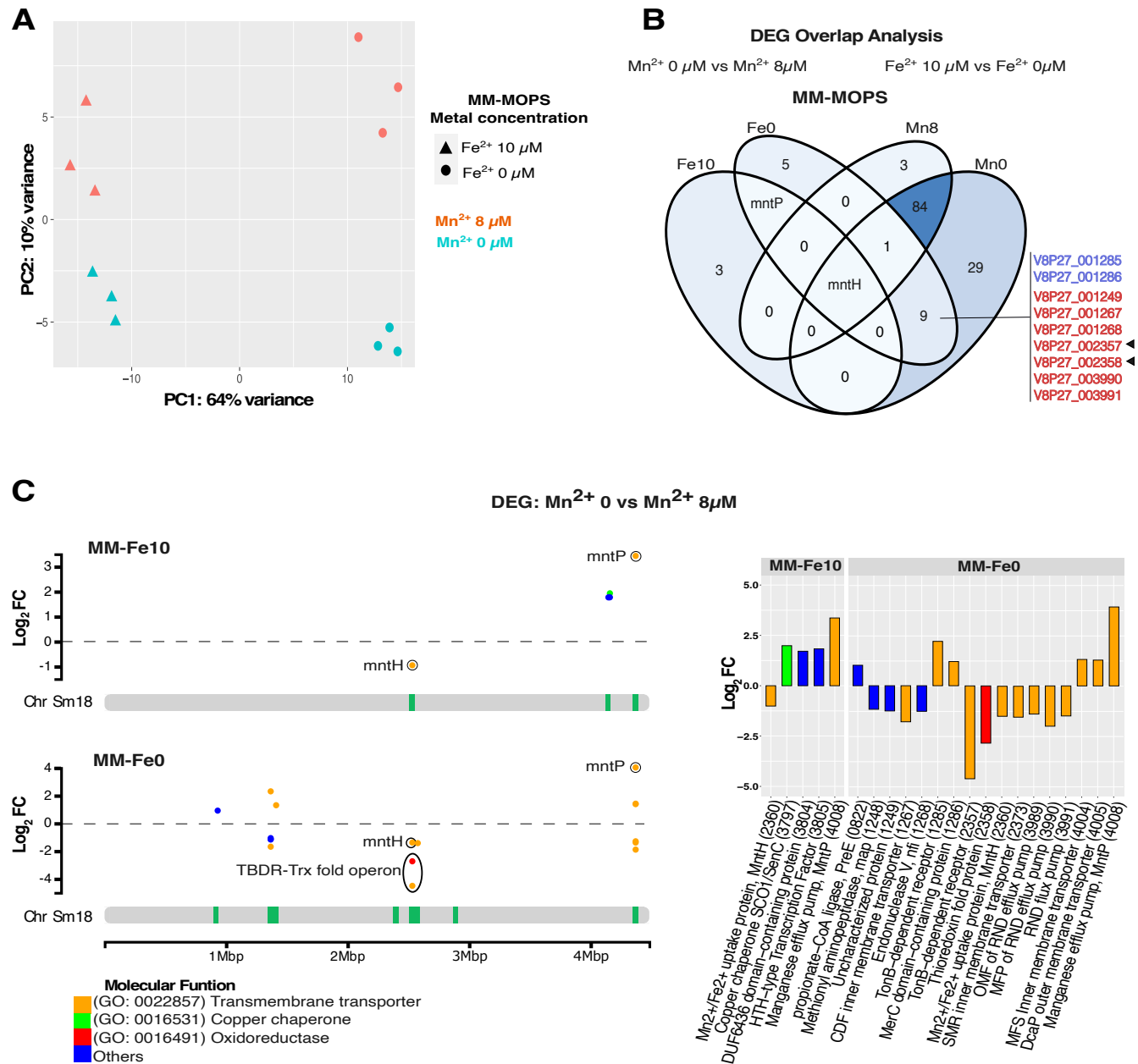
A
PC2: 10% variance
PC1: 64% variance
MM-MOPS
Metal concentration
Fe2+ 10 μM
Fe2+ 0 μM
Mn2+ 8 μM
Mn2+ 0 μM
B
DEG Overlap Analysis
Mn2+ 0 μM vs Mn2+ 8μM
Fe2+ 10 μM vs Fe2+ 0μM
MM-MOPS
Fe10
Fe0
Mn8
Mn0
mntP
mntH
V8P27_001285
V8P27_001286
V8P27_001249
V8P27_001267
V8P27_001268
V8P27_002357
V8P27_002358
V8P27_003990
V8P27_003991
C
DEG: Mn2+ 0 vs Mn2+ 8μM
MM-Fe10
MM-Fe0
Log2FC
mntP
mntH
Chr Sm18
TBDR-Trx fold operon
1Mbp
2Mbp
3Mbp
4Mbp
Molecular Funtion
(GO: 0022857) Transmembrane transporter
(GO: 0016531) Copper chaperone
(GO: 0016491) Oxidoreductase
Others
Mn2+/Fe2+ uptake protein, MntH (2360)
Copper chaperone SCO1/SenC (3797)
DUF6436 domain-containing protein (3804)
HTH-type Transcription Factor (3805)
Manganese efflux pump, MntP (4008)
propionate-CoA ligase, PreE (0822)
Methionyl aminopeptidase, map (1248)
Uncharacterized protein (1249)
CDF inner membrane transporter (1267)
Endonuclease V, nfi (1268)
TonB-dependent receptor (1285)
TonB-containing protein (1286)
MerC domain-containing protein (2357)
Thioredoxin fold protein (2358)
Mn2+/Fe2+ uptake protein, MntH (2360)
SMR inner membrane transporter (2373)
OMF of RND efflux pump (3989)
MFP of RND efflux pump (3990)
RND flux pump (3991)
MFS Inner membrane transporter (4004)
DcaP outer membrane transporter (4005)
Manganese efflux pump, MntP (4008)

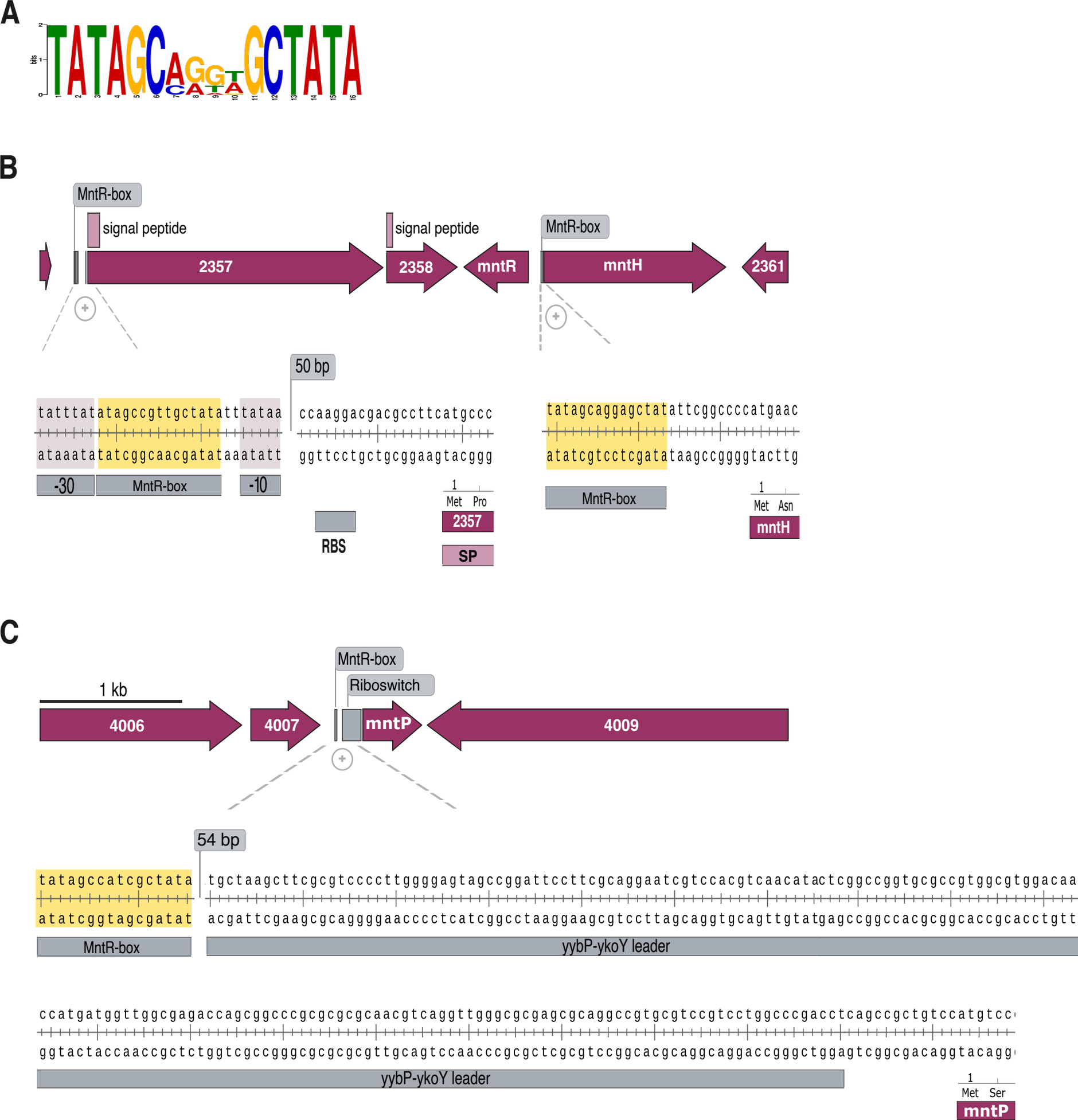
A
bits
B
MntR-box
signal peptide
signal peptide
MntR-box
2357
2358
mntR
mntH
2361
50 bp
tatttatatagccgttgctatatttataa
ccaaggacgacgccttcatgccc
ataaatatatcggcaacgatataaatatt
ggttcctgctgcggaagtacggg
tatagcaggagctatattcggccccatgaac
atatcgtcctcgatataagccggggtacttg
-30
MntR-box
-10
1
Met Pro
2357
RBS
SP
MntR-box
1
Met Asn
mntH
C
1 kb
MntR-box
Riboswitch
4006
4007
mntP
4009
54 bp
tatagccatcgctata
tgctaagcttcgcgtccccttggggagtagccggattccttcgcaggaatcgtccacgtcaacatactcggccggtgcgccgtggcgtggacaa
atatcggtagcgatat
acgattcgaagcgcaggggaacccctcatcggcctaaggaagcgtccttagcaggtgcagttgtatgagccggccacgcggcaccgcacctgtt
MntR-box
yybP-ykoY leader
ccatgatggttggcgagaccagcggcccgcgcgcgcaacgtcaggttgggcgcgagcgcaggccgtgcgtccgtcctggcccgacctcagccgctgtccatgtcc
ggtactaccaaccgctctggtcgccgggcgcgcgcgttgcagtccaacccgcgctcgcgtccggcacgcaggcaggaccgggctggagtcggcgacaggtacagg
yybP-ykoY leader
1
Met Ser
mntP

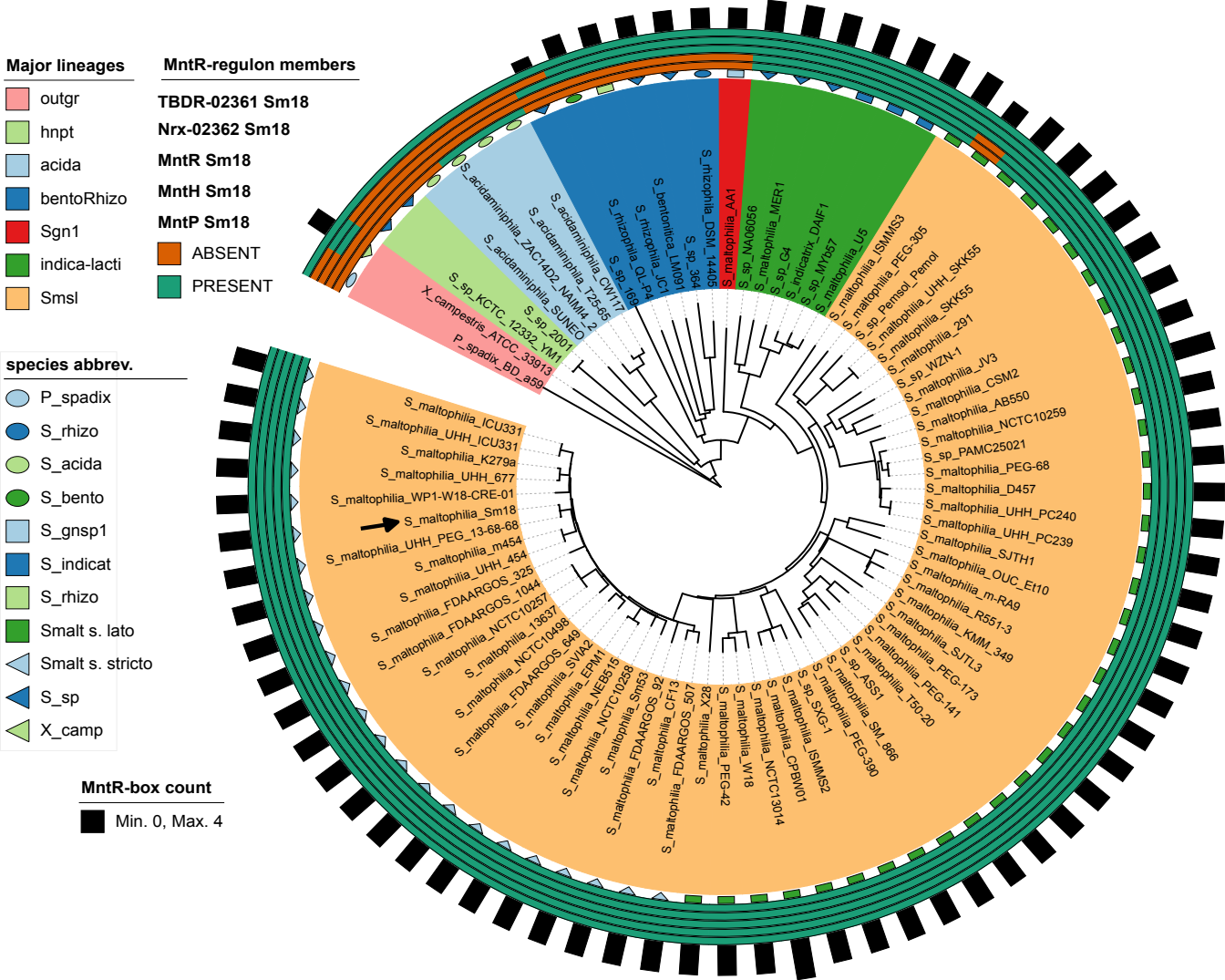
Major lineages
outgr
hnpt
acida
bentoRhizo
Sgn1
indica-lacti
Smsl
MntR-regulon members
TBDR-02361 Sm18
Nrx-02362 Sm18
MntR Sm18
MntH Sm18
MntP Sm18
ABSENT
PRESENT
species abbrev.
P_spadix
S_rhizo
S_acida
S_bento
S_gnsp1
S_indicat
S_rhizo
Smalt s. lato
Smalt s. stricto
S_sp
X_camp
MntR-box count
Min. 0, Max. 4
S_maltophilia_AA1
S_sp_NA06056
S_maltophilia_MER1
S_sp_G4
S_indicatrix_DAIF1
S_sp_MYb57
S_maltophilia_U5
S_maltophilia_ISMMS3
S_maltophilia_PEG-305
S_sp_Pemsol_Pemol
S_maltophilia_UHH_SKK55
S_maltophilia_SKK55
S_maltophilia_291
S_sp_WZN-1
S_maltophilia_JV3
S_maltophilia_CSM2
S_maltophilia_AB550
S_maltophilia_NCTC10259
S_sp_PAMC25021
S_maltophilia_PEG-68
S_maltophilia_D457
S_maltophilia_UHH_PC240
S_maltophilia_UHH_PC239
S_maltophilia_SJTH1
S_maltophilia_OUC_Et10
S_maltophilia_m-RA9
S_maltophilia_R551-3
S_maltophilia_KMM_349
S_maltophilia_SJTL3
S_maltophilia_PEG-173
S_maltophilia_PEG-141
S_maltophilia_T50-20
S_maltophilia_SM_866
S_sp_ASS1
S_maltophilia_PEG-390
S_sp_SXG-1
S_maltophilia_ISMMS2
S_maltophilia_CPBW01
S_maltophilia_NCTC13014
S_maltophilia_W18
S_maltophilia_PEG-42
S_maltophilia_X28
S_maltophilia_FDAARGOS_507
S_maltophilia_CF13
S_maltophilia_FDAARGOS_92
S_maltophilia_Sm53
S_maltophilia_FDAARGOS_1258
S_maltophilia_NEB516
S_maltophilia_EPM1
S_maltophilia_SVIA2
S_maltophilia_FDAARGOS_649
S_maltophilia_NCTC10498
S_maltophilia_13637
S_maltophilia_NCTC10257
S_maltophilia_FDAARGOS_1044
S_maltophilia_FDAARGOS_325
S_maltophilia_UHH_454
S_maltophilia_m454
S_maltophilia_UHH_PEG_13-68-68
S_maltophilia_Sm18
S_maltophilia_WP1-W18-CRE-01
S_maltophilia_UHH_677
S_maltophilia_K279a
S_maltophilia_UHH_ICU331
S_maltophilia_ICU331
S_rhizophilia_DSM_14405
S_sp_364
S_bentonitica_LMd001
S_rhizophilia_JC1
S_rhizophilia_QL-P4
S_sp_169
S_rhizophilia_CW117
S_acidaminiphilia_CW117
S_acidaminiphilia_T25-65
S_acidaminiphilia_NAIM14_2
S_acidaminiphilia_SUNEO
S_sp_2001
S_sp_KCTC_12332_YM1
X_campestris_ATCC_33913
P_spadix_BD_a59

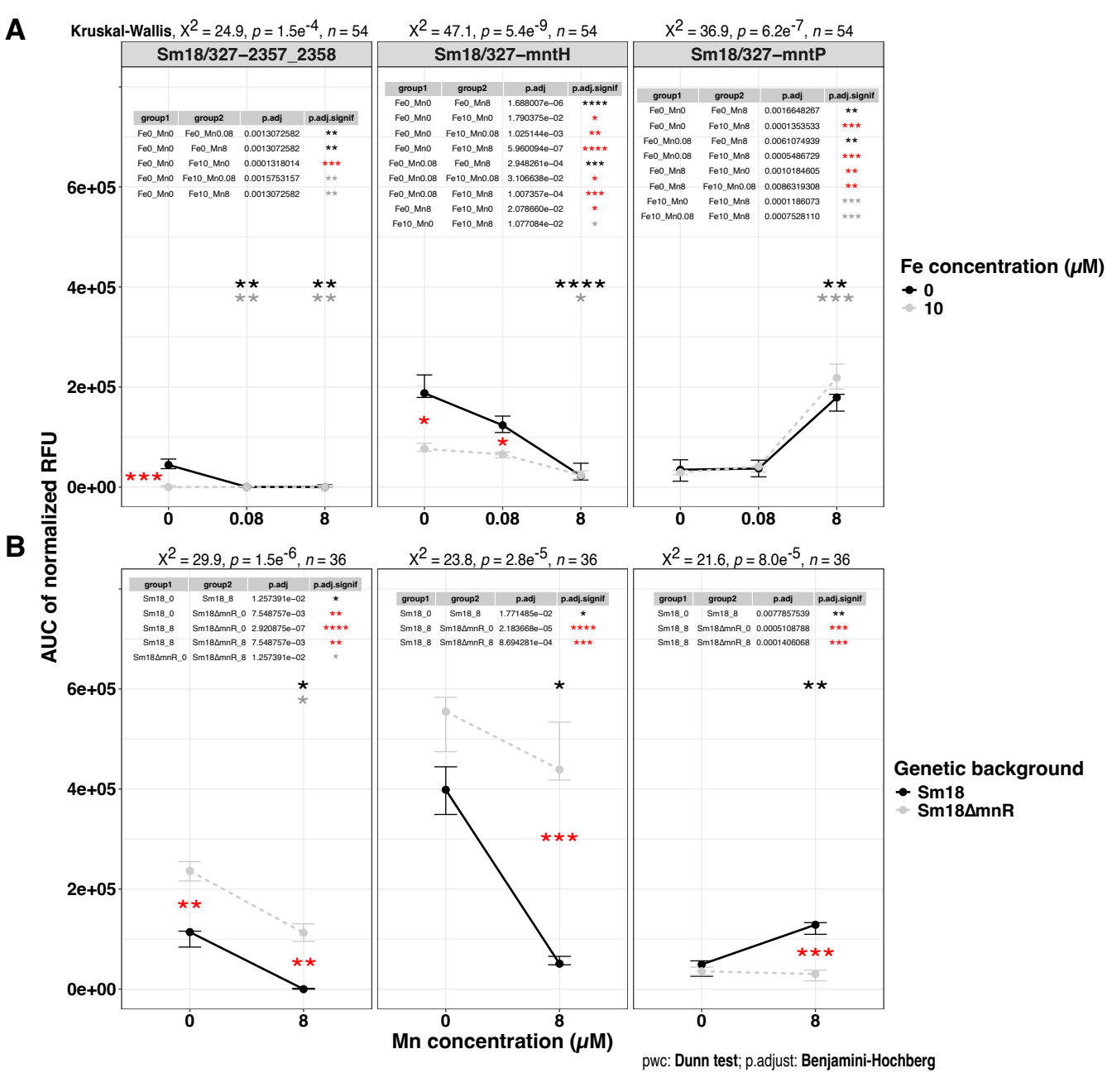
A
Kruskal-Wallis, X^2 = 24.9, p = 1.5e^{-4}, n = 54
X^2 = 47.1, p = 5.4e^{-9}, n = 54
X^2 = 36.9, p = 6.2e^{-7}, n = 54
Sm18/327−2357_2358
Sm18/327−mntH
Sm18/327−mntP
group1 group2 p.adj p.adj.signif
Fe0_Mn0 Fe0_Mn0.08 0.0013072582 **
Fe0_Mn0 Fe0_Mn8 0.0013072582 **
Fe0_Mn0 Fe10_Mn0 0.0001318014 ***
Fe0_Mn0 Fe10_Mn0.08 0.0015753157 **
Fe0_Mn0 Fe10_Mn8 0.0013072582 **
group1 group2 p.adj p.adj.signif
Fe0_Mn0 Fe0_Mn8 1.688007e−06 ****
Fe0_Mn0 Fe10_Mn0 1.790375e−02 *
Fe0_Mn0 Fe10_Mn0.08 1.025144e−03 **
Fe0_Mn0 Fe10_Mn8 5.960094e−07 ****
Fe0_Mn0.08 Fe0_Mn8 2.948261e−04 ***
Fe0_Mn0.08 Fe10_Mn0.08 3.106638e−02 *
Fe0_Mn0.08 Fe10_Mn8 1.007357e−04 ***
Fe0_Mn8 Fe10_Mn0 2.078660e−02 *
Fe10_Mn0 Fe10_Mn8 1.077084e−02 *
group1 group2 p.adj p.adj.signif
Fe0_Mn0 Fe0_Mn8 0.0016648267 **
Fe0_Mn0 Fe10_Mn8 0.0001353533 ***
Fe0_Mn0.08 Fe0_Mn8 0.0061074939 **
Fe0_Mn0.08 Fe10_Mn8 0.0005486729 ***
Fe0_Mn8 Fe10_Mn0 0.0010184605 **
Fe0_Mn8 Fe10_Mn0.08 0.0086319308 **
Fe10_Mn0 Fe10_Mn8 0.0001186073 ***
Fe10_Mn0.08 Fe10_Mn8 0.0007528110 ***
Fe concentration (μM)
0
10
B
X^2 = 29.9, p = 1.5e^{-6}, n = 36
X^2 = 23.8, p = 2.8e^{-5}, n = 36
X^2 = 21.6, p = 8.0e^{-5}, n = 36
group1 group2 p.adj p.adj.signif
Sm18_0 Sm18_8 1.257391e−02 *
Sm18_0 Sm18ΔmnR_0 7.548757e−03 **
Sm18_8 Sm18ΔmnR_0 2.920875e−07 ****
Sm18_8 Sm18ΔmnR_8 7.548757e−03 **
Sm18ΔmnR_0 Sm18ΔmnR_8 1.257391e−02 *
group1 group2 p.adj p.adj.signif
Sm18_0 Sm18_8 1.771485e−02 *
Sm18_8 Sm18ΔmnR_0 2.183668e−05 ****
Sm18_8 Sm18ΔmnR_8 8.694281e−04 ***
group1 group2 p.adj p.adj.signif
Sm18_0 Sm18_8 0.0077857539 **
Sm18_8 Sm18ΔmnR_0 0.0005108788 ***
Sm18_8 Sm18ΔmnR_8 0.0001406068 ***
AUC of normalized RFU
6e+05
4e+05
2e+05
0e+00
0
0.08
8
Mn concentration (μM)
Genetic background
Sm18
Sm18ΔmnR
pwc: Dunn test; p.adjust: Benjamini-Hochberg

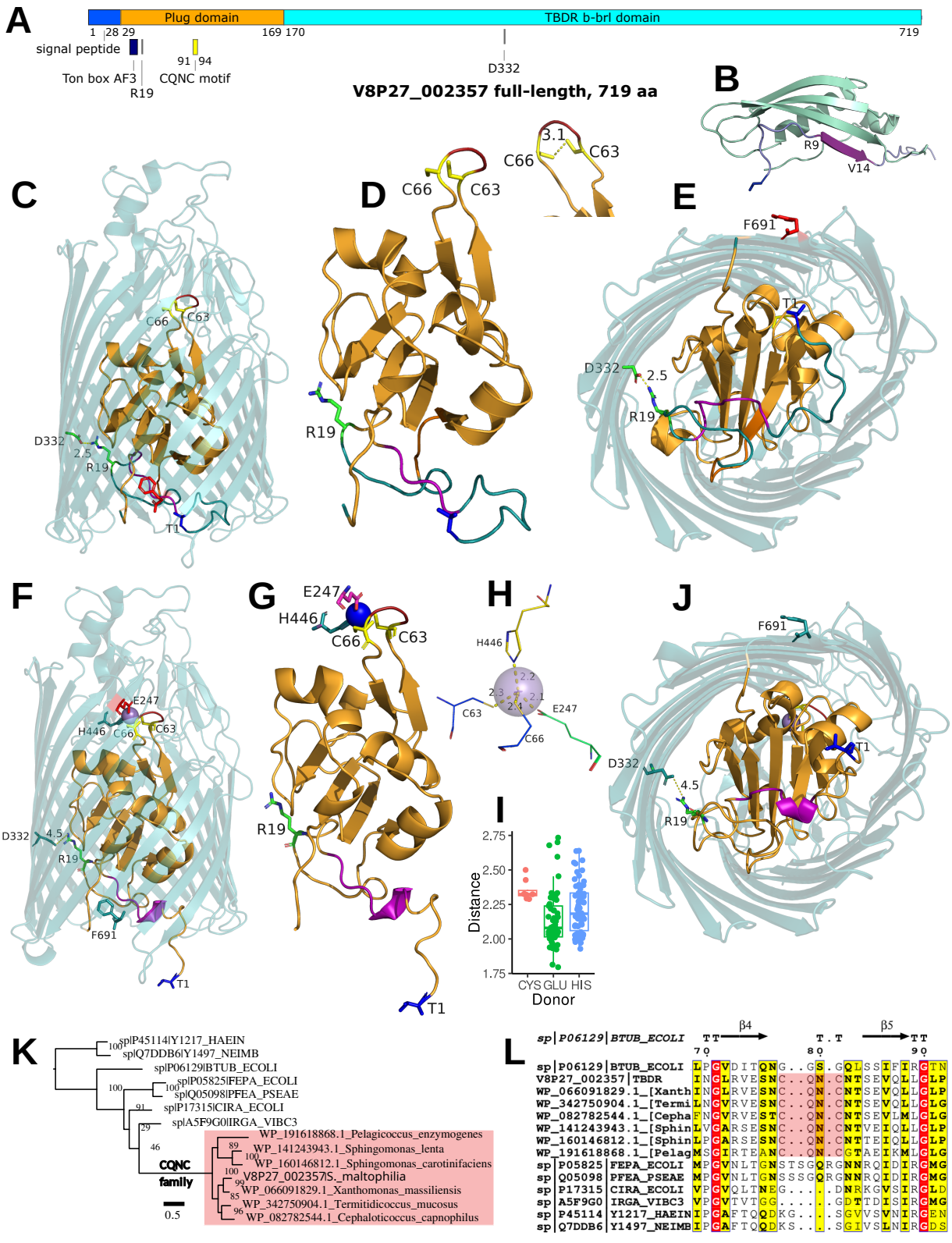
A
Plug domain
TBDR b-brl domain
1 28 29
169 170
719
signal peptide
91 94
Ton box AF3
CQNC motif
R19
D332
V8P27_002357 full-length, 719 aa
B
R9
V14
C
C66
C63
D332
2.5
R19
T1
D
C66
C63
3.1
R19
E
F691
T1
D332
2.5
R19
F
E247
H446
C66
C63
D332
4.5
R19
F691
T1
G
E247
H446
C66
C63
R19
T1
H
H446
C63
E247
C66
D332
I
Distance
CYS GLU HIS
Donor
J
F691
T1
D332
4.5
R19
K
sp|P45114|Y1217_HAEIN
sp|Q7DDB6|Y1497_NEIMB
sp|P06129|BTUB_ECOLI
sp|P05825|FEPA_ECOLI
sp|Q05098|PFEA_PSEAE
sp|P17315|CIRA_ECOLI
sp|A5F9G0|IRGA_VIBC3
WP_191618868.1_Pelagicoccus_enzymogenes
WP_141243943.1_Sphingomonas_lenta
WP_160146812.1_Sphingomonas_carotinifaciens
V8P27_002357|S._maltophilia
WP_066091829.1_Xanthomonas_massiliensis
WP_342750904.1_Termitidicoccus_mucosus
WP_082782544.1_Cephaloticoccus_capnophilus
CQNC family
0.5
L
β4
β5
sp|P06129|BTUB_ECOLI
V8P27_002357|TBDR
WP_066091829.1_[Xanth
WP_342750904.1_[Termi
WP_082782544.1_[Cepha
WP_141243943.1_[Sphin
WP_160146812.1_[Sphin
WP_191618868.1_[Pelag
sp|P05825|FEPA_ECOLI
sp|Q05098|PFEA_PSEAE
sp|P17315|CIRA_ECOLI
sp|A5F9G0|IRGA_VIBC3
sp|P45114|Y1217_HAEIN
sp|Q7DDB6|Y1497_NEIMB

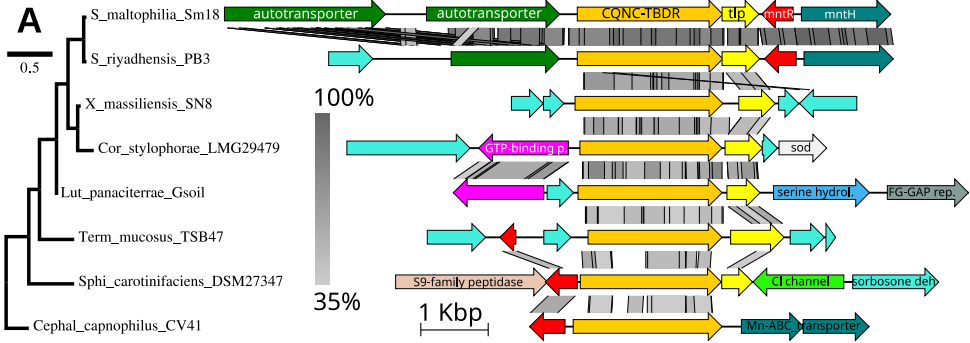

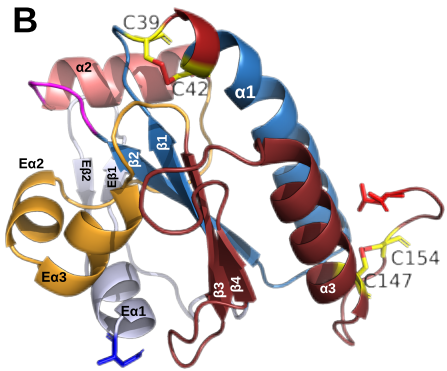

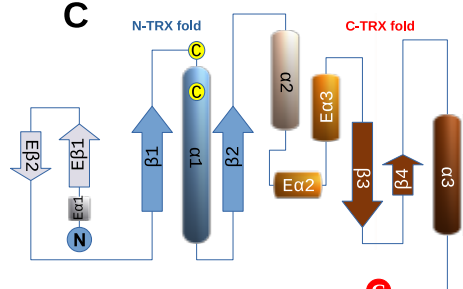

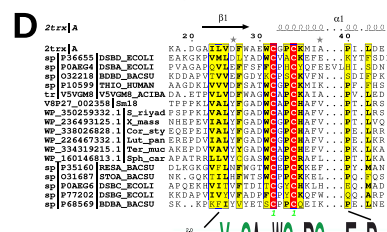

pTFPs associated with CQNQ-type TBDRs

Profile: Y[FYC]GA[DS]WC[AG]PCH[AE]F[VL]P

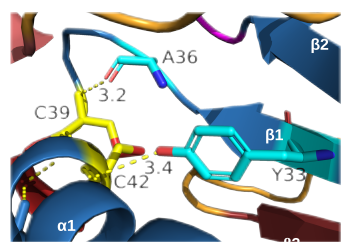

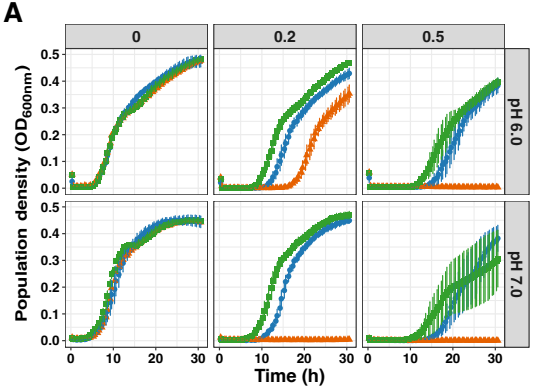
A
0
0.2
0.5
pH 6.0
pH 7.0
Population density (OD600nm)
Time (h)

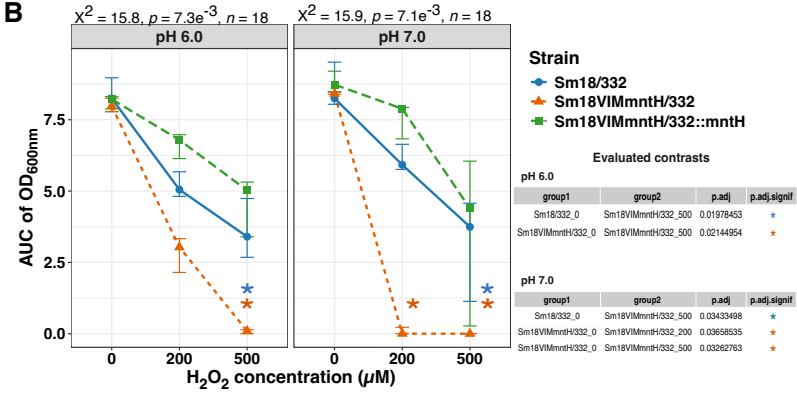
B
X2 = 15.8, p = 7.3e-3, n = 18
X2 = 15.9, p = 7.1e-3, n = 18
pH 6.0
pH 7.0
AUC of OD600nm
H2O2 concentration (μM)
Strain
Sm18/332
Sm18VIMmntH/332
Sm18VIMmntH/332::mntH
Evaluated contrasts
pH 6.0
group1 group2 p.adj p.adj.signif
Sm18/332_0 Sm18VIMmntH/332_500 0.01978453 *
Sm18VIMmntH/332_0 Sm18VIMmntH/332_500 0.02144954 *
pH 7.0
group1 group2 p.adj p.adj.signif
Sm18/332_0 Sm18VIMmntH/332_500 0.03433498 *
Sm18VIMmntH/332_0 Sm18VIMmntH/332_200 0.03658535 *
Sm18VIMmntH/332_0 Sm18VIMmntH/332_500 0.03262763 *

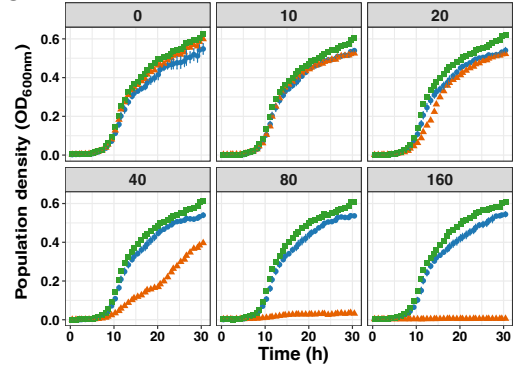
C
0
10
20
40
80
160
Population density (OD600nm)
Time (h)

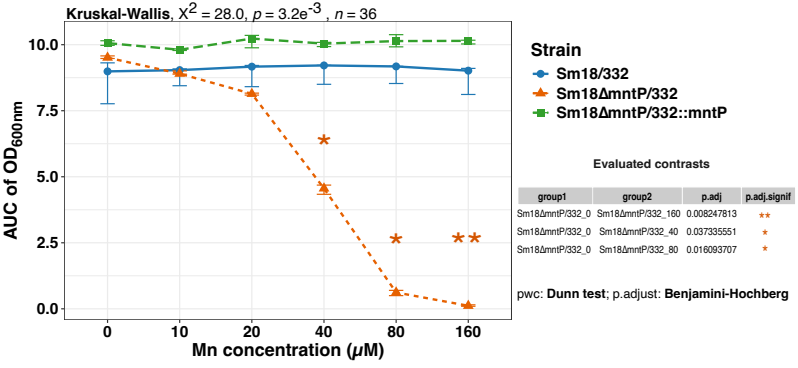
D
Kruskal-Wallis, X2 = 28.0, p = 3.2e-3, n = 36
AUC of OD600nm
Mn concentration (μM)
Strain
Sm18/332
Sm18ΔmntP/332
Sm18ΔmntP/332::mntP
Evaluated contrasts
group1 group2 p.adj p.adj.signif
Sm18ΔmntP/332_0 Sm18ΔmntP/332_160 0.008247813 **
Sm18ΔmntP/332_0 Sm18ΔmntP/332_40 0.037335551 *
Sm18ΔmntP/332_0 Sm18ΔmntP/332_80 0.016093707 *
pwc: Dunn test; p.adjust: Benjamini-Hochberg

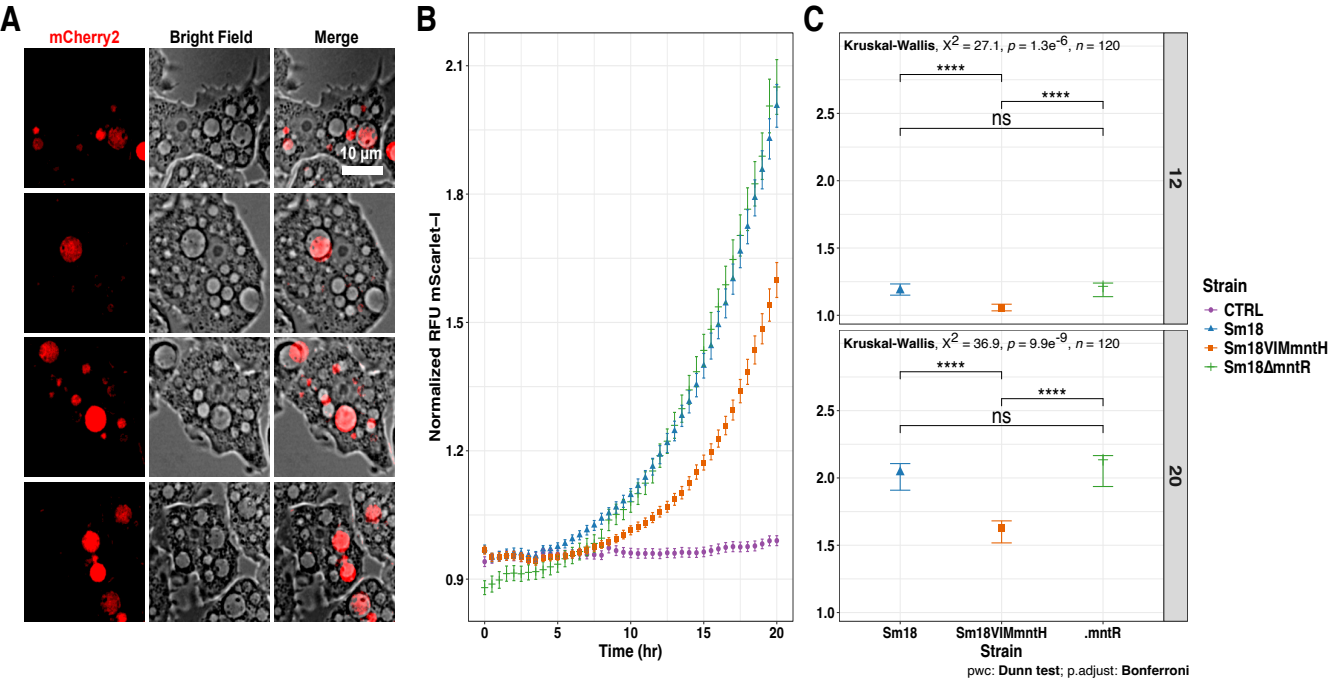
A
mCherry2
Bright Field
Merge
10 µm
B
Normalized RFU mScarlet−I
Time (hr)
C
Kruskal-Wallis, X2 = 27.1, p = 1.3e-6, n = 120
Kruskal-Wallis, X2 = 36.9, p = 9.9e-9, n = 120
****
ns
12
20
Sm18
Sm18VIMmntH
.mntR
Strain
pwc: Dunn test; p.adjust: Bonferroni
Strain
CTRL
Sm18
Sm18VIMmntH
Sm18ΔmntR